Estimation of Transmitted Differential Phase on Dual-Polarization Radars

D. S. ZRNIĆ[a,b,c] AND V. M. MELNIKOV[d,a]

[a] *NOAA/OAR/National Severe Storms Laboratory, Norman, Oklahoma*
[b] *School of Meteorology, University of Oklahoma, Norman, Oklahoma*
[c] *School of Electrical and Computer Engineering, University of Oklahoma, Norman, Oklahoma*
[d] *Cooperative Institute for Severe and High-Impact Weather Research and Operations, University of Oklahoma, Norman, Oklahoma*

(Manuscript received 12 February 2022, in final form 21 July 2023, accepted 25 July 2023)

ABSTRACT: A measurement procedure to determine transmitted differential phase between horizontally and vertically polarized radiation of a dual-polarization radar is presented. It is applicable to radars that transmit and receive simultaneously horizontally and vertically (SHV) polarized waves. The method relies solely on weather data with no instrument intrusions whatsoever. It takes data at vertical incidence while the antenna rotates in azimuth. That way, a large number of samples is collected to reduce statistical errors in estimates. The theory indicates that the transmitted differential phase appears prominently in the backscatter signals off the melting layer. That and relations between various elements of the backscattering matrix are used to derive a set of nonlinear equations whereby the differential phase on transmission is one of the unknowns. Steps for solving these equations are presented as well as a demonstration of the results on radar data. A simplified algorithm that bypasses the coupled nonlinear equations is exposed. Conditions under which the simplification can be applied are presented. These restrict the range of the transmitted differential phase for which the simplified procedure may be applied.

KEYWORDS: Data quality control; Radars/radar observations; Weather radar signal processing

1. Introduction

Advancements in dual-polarization radar and its inclusion into the operational arena brought opportunities and challenges. Among the former are improved quantitative measurements of rain (Zhang et al. 2020) and snow (Bukovčić et al. 2020), separation of meteorological returns from other scatterers (Krause 2016), classification of returns (Park et al. 2009), and so on. Moreover, research suggests that polarimetry can help improve assimilation of radar data into numerical weather prediction (NWP) models (e.g., Carlin et al. 2017; Zhang et al. 2019) and even guide these toward more accurate prediction (Ryzhkov et al. 2020). The challenges are in calibrations of various polarimetric variables. Observations at vertical incidence can meet some of these challenges.

A good way to calibrate differential reflectivity, Z_{DR} is via measurements at vertical incidence (Gorgucci et al. 1999; Borowska and Zrnić 2012). Moisseev et al. (2002) estimate the bias of the copolar correlation coefficient ρ_{hv} and the linear depolarization ratio L_{dr} from vertical observations in light rain. The German weather service monitors absolute calibration of their polarimetric radars by measurements at vertical incidence and collocated disdrometers (Frech et al. 2017). They also compare these measurements with those collected with a micro rain radar (Peters et al. 2005).

The preferred dual-polarization mode by national weather services in United States, Germany, Canada, United Kingdom, Japan, Finland, Italy, and so on, is simultaneous transmission and reception of the horizontally and vertically (SHV) polarized waves. The reasons are several (Doviak et al. 2000; Doviak and Zrnić 1998). In the SHV mode reflectivity Z, Z_{DR}, ρ_{hv}, and propagation differential phase Φ_{DP} are measured. However, under special circumstances the circular depolarization ratio (CDR) or its proxies can be estimated. From these, information about particle type and shape can be extracted (Matrosov 2004; Melnikov and Matrosov 2013; Ryzhkov et al. 2017). Matrosov (2004) proposes to estimate CDR; his estimator requires that differential phase on transmission β and receiver differential phase γ be related as $\beta = -\gamma = 90°$. He also advocates a slightly different estimator requiring that $\beta + \gamma = 0$. Knowledge of β and γ is needed to determine how close the proposed estimators would approximate the true CDR. Ryzhkov et al. (2017) introduce the depolarization ratio DR, a proxy to CDR uniquely related to Z (at horizontal polarization), Z_{DR}, ρ_{hv}, and Φ_{DP}. DR does not carry new information; rather, it combines the existing variables into one from which some hydrometeor types like rimed snow can be readily separated from aggregates. These authors favor DR for the SHV mode because "it is likely that the relative differences of DR between various types of snow/ice may not be much affected by the uncertainty in β, at least in a qualitative sense. We showed that these differences are maximized if the radar transmits the wave with truly circular polarization that motivates the utilization of a phase shifter for controlling β." True CDR is independent of particle orientation in the polarization plane and generally may have practical applications like (ad lib quotation from Ryzhkov et al. 2017) "detection of hail and its size, discrimination between various habits of ice, and possible identification and quantification of riming." These capabilities are hard to achieve with the four polarimetric variables available in the SHV mode. The first polarimetric identification of hail was through observations of increased CDR (Barge 1974). Even if not used for adjusting/computing CDR or its proxies, β in combination with γ and Φ_{DP} has

Corresponding author: Dusan Zrnić, dusan.zrnic@noaa.gov

DOI: 10.1175/JTECH-D-22-0014.1

a strong influence on biases of polarimetric variables in the SHV mode (Zrnić et al. 2010; Galletti and Zrnić 2011).

Although quantifying β can be useful, on most polarimetric weather radars it cannot be measured or easily changed. Notable exception is the fully agile polarimetric radar belonging to the German Aerospace Center [Deutsches Zentrum für Luft- und Raumfahrt (DLR)] that can transmit any elliptical polarization (Schroth et al. 1988). Melnikov et al. (2015) estimate β of a WSR-88D from insects returns. They developed a scattering model of EM waves whereby β is one of the fitted parameters. Their model reproduces the observed asymmetric azimuthal patterns of the polarimetric variables fairly well. Moreover, Melnikov (2020) demonstrates that β induces differential phase on returns from plate crystals at vertical incidence (in the SHV mode).

Herein, we present a method to determine β from returns off the melting layer at vertical incidence. We start with the background explaining the significance of β (section 2). The theory behind the measurement we expose in section 3 and demonstrate on measurements in section 4. Discussion we reserve for section 5 and conclude with section 6. Significant background material and a backscattering model off the melting layer at vertical incidence are in the appendix.

2. Background

We briefly summarize the importance of the transmitted differential phase on radars operating in the SHV mode.

a. Effects on bias in polarimetric variables

Differential phases from various sources affect strongly the values of Z_{DR} (Zrnić et al. 2010) and ρ_{hv} (Galletti and Zrnić 2011). Moreover, β has a similar effect on these two variables. Therefore, constraining the bias in one automatically limits the bias in the other variable. The equation for Z_{DR} bias [Zrnić et al. 2010, their (15)] is

$$\delta Z_{DR} \approx 20\log(e)W\{-2\sin\beta\sin\gamma + \rho_{hv}[Z_{dr}^{-1/2}\cos(\Phi_{DP}+\beta+\gamma) - Z_{dr}^{1/2}\cos(\Phi_{DP}+\beta-\gamma)]\}, \quad \text{(dB)} \tag{1}$$

where $W = \int_\Omega F_{hh}^3|F_{hv}|\,d\Omega / \int_\Omega F_{hh}^4\,d\Omega$. Here, F_{hh} is the amplitude antenna pattern of the main lobe for horizontal polarization. The $|F_{hv}|$ is absolute value of cross-polar pattern (the H polarization generated by the intended V polarization) and the bias is correct to first order in F_{hv}; that is, (1) contains $|F_{hv}|$ raised to the first power but the higher-order powers (second, third, and fourth) are ignored. Here, Ω is the solid angle, and integration is over the main lobe. The bias δZ_{DR} is in decibels but the differential reflectivity Z_{dr} on the right side of (1) is in linear scale.

Depending on how the phases β, γ, and Φ_{DP} in (1) add, δZ_{DR} may exhibit large variations. Consider $\Phi_{DP} = 0°$ as would be at the first range location where the beam penetrates precipitation. Then (1) indicates δZ_{DR} is maximum negative if $\beta = \pm 90°$, $\gamma = \pm 90°$ (see also Zrnić et al. 2010, Fig. 3). Maximum positive value occurs if $\beta = \pm 90°$ and $\gamma = \mp 90°$. There is no bias if $\beta = 0°$, $\gamma = \pm 90°$ or $\beta = \pm 90°$, $\gamma = 0°$.

Significance of β for bias consideration is twofold.

1) If the radar has a phase shifter in the transmission path it may be possible to adjust β and minimize bias at distances close to the radar where observations are most important. Say the bias is minimized at the range of first penetration into rain where Φ_{DP} is zero. According to (1), with the increase in Φ_{DP} the bias would rise.
2) We can estimate from (1) the value of bias. Take again rain closest to the radar where Φ_{DP} is zero; ρ_{hv} would be close to one and the typical range of Z_{dr} (linear units) in rain would be between 1 and about 2 (Straka et al. 2000, Fig. 2a). The system differential phase consists of β and γ; that is,

$$\Phi_{DPsys} = \beta + \gamma, \tag{2}$$

and is easily measured from the returns closest to the radar. Knowledge of these phases and ρ_{hv} and Z_{dr} would enable researchers to assess bias at farther distances and censor data deemed corrupt.

b. Depolarization ratios

Matrosov (2004) suggests setting $\gamma = -\beta$ to generate the elliptical depolarization ratio EDR, i.e., the power ratio of two orthogonally polarized returns; one has left-hand elliptical (LHE) polarization the other right-hand elliptical (RHE) polarization. Orthogonality maximizes contrast in the powers of these returns. If $\gamma = -\beta = 0$, EDR changes to the slant linear depolarization ratio (Chandrasekar et al. 1994). Adjusting γ is very simple by digitally altering the relative phase between the two receivers. This, however, is not the case with β. But knowing β is required to determine EDR. From the simplified version of depolarization ratio D_{dr} [set $\gamma = -\beta$ in (A15) of the appendix], EDR becomes

$$\text{EDR} = \frac{\langle|S_{hh} + 2jS_{hv}\sin\beta - S_{vv}|^2\rangle}{\langle|S_{hh} + 2S_{hv}\cos\beta + S_{vv}|^2\rangle}, \tag{3}$$

where the backscattering matrix terms are denoted with the usual S_{ij} symbols. Note that if β shifts by 180° EDR in (3) becomes a ratio of left-handed to right-handed or vice versa elliptically polarized returns.

From (3) it follows that if $\beta = \pm 90°$ the EDR changes to the circular depolarization ratio, CDR defined by

$$\text{CDR} = \frac{\langle|S_{hh} \pm 2jS_{hv} - S_{vv}|^2\rangle}{\langle|S_{hh} + S_{vv}|^2\rangle}. \tag{4}$$

Matrosov et al. (2001) predict dependence of slant linear and circular depolarization ratios from crystal types on the elevation angle of the antenna beam. Moreover, they include a study of two elliptical polarizations motivated by a specific polarimetric radar design. The slant linear depolarization ratios' dependence on antenna elevation exhibits remarkable signatures of some crystal habits (Reinking et al. 2002, their Fig. 5). These are backed by model results (Reinking et al. 2002, their

Fig. 3). The reported success inspired application of slant 45° technique for measurements with a 3-mm-wavelength radar (Matrosov et al. 2012). That study proves "the depolarization measurements can be used for identification of dominant ice particle habits and estimation of their shapes, and thus for future studies of ice hydrometeor microphysics and prevalent particle growth processes (e.g., vapor deposition vs aggregation)." More recently Matrosov et al. (2017) used a fully polarimetric (transmits H and receives both then transmits V and receives both, etc.) radar (8.5-mm wavelength) to obtain a proxy circular depolarization ratio $D_{\rm dr}$ (see the appendix) and infer axis ratios of snow particles. The technique requires a special radar design with a full control of the transmitted polarization state. Most weather polarization radars have no controls nor means to measure β. Observations of $D_{\rm dr}$ dependence on elevation would benefit if β were known because then γ could be adjusted in the receiver to somewhat optimize $D_{\rm dr}$ (within the constraint of a fixed β).

Cao et al. (2017) propose hardware changes for adjusting β to produce circular polarization (i.e., impose $\beta = \pm 90°$). They demonstrate this by inserting a variable high power phase shifter into one of the channels. This enables measurement of true CDR at locations where $\Phi_{\rm DP}$ is negligible. At other locations a more useful and meaningful estimate of $D_{\rm dr}$ ensues. Although it is possible to estimate β with hardware, inclusion of instruments and components needed for measurements changes the signal path in the radar and the effects of this change are very difficult to account for. Measurement on data avoids this interference with the radar system. Moreover, unlike the hardware measurement on signals prior to reaching the antenna the estimate from data includes paths missed by the engineering method (e.g., from couplers to the antenna and out).

In summary, the conditions $\beta = 0°$, $\gamma = \pm 90°$ or $\beta = \pm 90°$, $\gamma = 0°$ reduce bias in $Z_{\rm DR}$, by itself $\beta = \pm 90°$ generates circular polarization useful for classification of precipitation, whereas the equality $\beta = -\gamma$ maximizes $D_{\rm dr}$ enabling separation of ice crystal types based on $D_{\rm dr}$'s dependence on antenna elevation. The three conditions on β are incompatible, hence cannot be satisfied at the same time. Nonetheless, these can be achieved sequentially provided that changing β is possible. This, however, is not practical on conventional radars because it would involve rapidly changing phase of high power transmitted signals. Quick change is possible on phased array radars (PAR) because it can be made on array elements. Herein, suggested measurements of β could be applied to PARs for verifying the values of the transmitted differential phases.

3. Theory

We derive a set of equations from which the phase difference between the transmitted horizontally polarized wave and the vertically polarized wave can be computed using measurements. The computation relies solely on data collected at vertical incidence. System differential phase, $\Phi_{\rm DPsys}$ calibration is an integral part of the procedure and measurements at two range locations are required: one in rain below bright band, the other in the bright band at the location of the minimum in the copolar correlation coefficient. From the measurement in rain we retrieve $\Phi_{\rm DPsys}$ and $Z_{\rm DR}$ (Gorgucci et al. 1999). We use measurements in the bright band and a physical constraint to construct a complete set of equations relating backscatter parameters to β.

The relation between received voltages ($V_{\rm hR}$, $V_{\rm vR}$) corresponding to the two polarized fields probing rain at vertical incidence and transmitter voltages is [appendix (A3)]

$$V_{\rm hR} = CS_{\rm hh}({\rm V}) \quad \text{and} \tag{5a}$$

$$V_{\rm vR} = CC_RC_Te^{j(\beta+\gamma)}S_{\rm hh}({\rm V}). \tag{5b}$$

Implicit in (5a) is that its right side is multiplied with the transmitter voltage for H (horizontal) polarization $V_{\rm hT} = (1{\rm V})$. The transmitter voltage for vertical (V) polarization $V_{\rm vT} = C_Te^{j\beta}$ (V) is on the right side of (5b). The constant C makes the two sides of (5) equal (in the absolute sense) and dimensionally consistent (see the appendix). Note that transmitter differential phase $\beta = \arg(V^*_{\rm hT}V_{\rm vT})$ and that the differential gain between voltages on transmission is C_T (a real number); γ is the differential phase of the receiving system, and C_R is the differential voltage gain of the receiver. Consequently, the system differential power gain $(C_RC_T)^2$ represents the bias in $Z_{\rm dr}$ (linear units). Herein, we abbreviate this bias with

$$A^2 = C_R^2C_T^2 = P_{\rm vR}/P_{\rm hR}, \tag{6}$$

where $P_{\rm vR}$ and $P_{\rm hR}$ are powers equal to the magnitude squared of the voltages in (5). We assume hydrometeors are homogeneously distributed and isotropic in any horizontal plane. Therefore, propagation of the H and V fields is equally affected causing $\Phi_{\rm DP}$ to be 0. The system differential phase $\Phi_{\rm DPsys}$ (2) is the $\arg(V^*_{\rm hR}V_{\rm vR})$ at any range in rain (at vertical incidence). Attenuations and dependence on range are omitted as these have no bearing on our method.

a. Derivation of equations

Consider a scattering model of the melting layer at vertical incidence whereby snowflakes are randomly oriented in the horizontal plane (i.e., plane of polarization). In the SHV mode, the equation relating voltages to the backscattering matrix is (see the appendix; Ryzhkov et al. 2017)

$$\begin{vmatrix} V_{\rm hM} \\ V_{\rm vM} \end{vmatrix} = C \begin{vmatrix} 1 & 0 \\ 0 & C_Re^{j\gamma} \end{vmatrix} \begin{vmatrix} e^{-j\Phi_{\rm DP}/2} & 0 \\ 0 & 1 \end{vmatrix} \begin{vmatrix} S_{\rm hh} & S_{\rm hv} \\ S_{\rm vh} & S_{\rm vv} \end{vmatrix} \begin{vmatrix} e^{-j\Phi_{\rm DP}/2} & 0 \\ 0 & 1 \end{vmatrix} \begin{vmatrix} 1 & \\ & C_Te^{j\beta} \end{vmatrix}, \tag{7}$$

where subscript M indicates melting layer. Reciprocity imposes $S_{\rm hv} = S_{\rm vh}$, and, with this condition, evaluating the matrices in (7) leads to the explicit expressions

$$\begin{aligned} V_{\rm hM} &= C(S_{\rm hh}e^{-j\Phi_{\rm DP}} + C_TS_{\rm hv}e^{-j\Phi_{\rm DP}/2+j\beta}) \quad \text{and} \\ V_{\rm vM} &= C(C_RS_{\rm hv}e^{-j\Phi_{\rm DP}/2+j\gamma} + C_RC_TS_{\rm vv}e^{j\beta+j\gamma}). \end{aligned} \tag{8}$$

This equation is almost identical to (A13) in Doviak et al. (2000) except that the sign on γ is negative. This choice

equates the system differential phase to $\beta - \gamma$, creating an unnecessary inconvenience.

Because snowflakes have uniform distribution of random orientation over 360° in the horizontal plane, the effects of propagation perpendicular to the horizontal plane are independent of the incident fields orientation. Therefore, at vertical incidence the two orthogonal fields experience equal phase shifts; hence, $\Phi_{DP} = 0$ (this also holds in rain). Moreover, homogeneity and isotropy impose the following relations at vertical incidence in the melting layer (appendix section b)

$$\langle |S_{hh}|^2 \rangle = \langle |S_{vv}|^2 \rangle \quad \text{and} \tag{9a}$$

$$\langle S_{hh} S_{hv}^* \rangle = \langle S_{vh} S_{vv}^* \rangle = 0, \tag{9b}$$

where the angle brackets denote ensemble average and the asterisk stands for complex conjugate.

Use (8) and (9a) to express the measured powers (P_{hM} and P_{vM}) at each polarization from the melting layer returns (indicated with the subscript M) in the H and V channels:

$$P_{hM} = C^2 \langle |S_{hh} + C_T S_{hv} e^{j\beta}|^2 \rangle = C^2 \langle |S_{hh}|^2 \rangle + C^2 C_T^2 \langle |S_{hv}|^2 \rangle \quad \text{and} \tag{10a}$$

$$\begin{aligned} P_{vM} &= C^2 \langle |C_R S_{hv} e^{j\gamma} + C_R C_T S_{vv} e^{j\beta + j\gamma}|^2 \rangle \\ &= C^2 C_R^2 \langle |S_{hv}|^2 \rangle + C^2 C_R^2 C_T^2 \langle |S_{hh}|^2 \rangle, \end{aligned} \tag{10b}$$

where the right sides are the consequence of randomly oriented snowflakes in the polarization plane (9a) and (9b) (appendix section b). An additional measurement in the melting layer is the cross correlation of the returns (8):

$$\begin{aligned} R_{hvM} = V_{hM}^* V_{vM} &= C^2 C_R C_T \langle S_{hh}^* S_{vv} \rangle e^{j\gamma + j\beta} \\ &+ C^2 C_R C_T \langle |S_{hv}|^2 \rangle e^{j\gamma - j\beta}. \end{aligned} \tag{11a}$$

The measured correlation coefficient corresponding to (11a) is by definition

$$\rho_{hvM} = \frac{R_{hvM}}{(P_{hM} P_{vM})^{1/2}} \tag{11b}$$

and will be frequently used. Multiply (11a) with $\exp(-j\Phi_{DPsys})$ to take γ out of the right side, and, to compact notation, introduce

$$D_M = \mathrm{Re}(R_{hvM} e^{-j\Phi_{DPsys}}) \text{ and } G_M = \mathrm{Im}(R_{hvM} e^{-j\Phi_{DPsys}}), \tag{11c}$$

thus generating

$$\begin{aligned} R_{hvM} e^{-j\Phi_{DPsys}} = D_M + jG_M &= C^2 C_R C_T \langle S_{hh}^* S_{vv} \rangle \\ &+ C^2 C_R C_T \langle |S_{hv}|^2 \rangle e^{-j2\beta}. \end{aligned} \tag{12}$$

By definition and using (9a)

$$\langle S_{hh}^* S_{vv} \rangle = \rho_{hvi} \langle |S_{hh}|^2 \rangle, \tag{13}$$

where the intrinsic correlation coefficient ρ_{hvi} is an unknown parameter and in this case a real number. Introduce ρ_{hvi} as per (13) and $A = C_R C_T$ from (6) into (12) to produce

$$D_M + jG_M = AC^2 \langle |S_{hh}|^2 \rangle \rho_{hvi} + AC^2 \langle |S_{hv}|^2 \rangle e^{-j2\beta}. \tag{14}$$

This equation is crucial for computing β. The left side comes from measurements, and the variables ρ_{hvi}, $C^2 \langle |S_{hh}|^2 \rangle$, and $C^2 \langle |S_{hv}|^2 \rangle$ on the right side are unknown. These are intrinsic to the melting layer and not directly measured. To compact (14), substitute

$$x = C^2 \langle |S_{hh}|^2 \rangle \quad \text{and} \tag{15a}$$

$$y = C^2 \langle |S_{hv}|^2 \rangle \tag{15b}$$

so that it becomes

$$D_M + jG_M = Ax\rho_{hvi} + Aye^{-j2\beta}. \tag{16}$$

The unknowns in (16) are x, y, and ρ_{hvi}. The procedure to determine these is as follows:

1) Drop the middle terms of (10a) and (10b).
2) Substitute x and y into the right terms of (10a) and (10b).
3) Substitute A^2 into the right term of (10b).
4) Subtract x from both sides of (10a).
5) Subtract $A^2 x$ from both sides of (10b).
6) Multiply the left terms and the right terms of the resulting equations.

This results in

$$(P_{hM} - x)(P_{vM} - A^2 x) = (Ay)^2. \tag{17}$$

Express the real and imaginary parts of (16) as

$$D_M - Ax\rho_{hvi} = Ay \cos 2\beta \quad \text{and} \tag{18a}$$

$$G_M = -Ay \sin 2\beta. \tag{18b}$$

Square the two sides of (18a) and (18b), and sum the results after applying $\sin^2(2\beta) + \cos^2(2\beta) = 1$ to get

$$(D_M - A\rho_{hvi} x)^2 + G_M^2 = (Ay)^2. \tag{19}$$

Note that the right side of (19) equals the right side of (17). Equate the two left sides to create the following quadratic equation in x:

$$\begin{aligned} &[(A\rho_{hvi})^2 - A^2] x^2 + (P_{vM} + P_{hM} A^2 - 2A\rho_{hvi} D_M) x \\ &- P_{hM} P_{vM} + D_M^2 + G_M^2 = 0. \end{aligned} \tag{20}$$

Because snowflakes have uniform distribution of orientation in the horizontal plane of the melting layer, the ρ_{hvi} (intrinsic) is related to the linear depolarization ratio L_{dr} via [see Ryzhkov and Zrnić 2019, their (3.48)]

$$\rho_{hvi} = 1 - 2L_{dr} = 1 - 2\langle |S_{hv}|^2 \rangle / \langle |S_{hh}|^2 \rangle = 1 - 2y/x, \tag{21a}$$

where

$$L_{dr} = \langle |S_{hv}|^2 \rangle / \langle |S_{hh}|^2 \rangle = y/x. \quad (21b)$$

Equations (17), (19), and (21a) form a set of *coupled nonlinear equations* relating ρ_{hvi}, x, and y. By combining (17) and (19) we eliminated y so that the set of nonlinear equation becomes (17), (20), and (21a).

b. Solution of the equations

The solution method we choose is a hybrid type, whereby we combine an analytic expression with a graph as follows. Consider $\rho_{hvi}(k)$ as a varying free parameter depending on the index k and with changing values between 0.5 and 1. These encompass typical ρ_{hvi} in melting snow between 0.88 and 0.985 [see Ryzhkov and Zrnić 2019, their Table 9.2, the subtable labeled $P(\rho_{hv})$ column for wet snow, WS]. Set the increment of $\rho_{hvi}(k)$ to 0.001; therefore, $\rho_{hvi}(k) = 0.5 + 0.001k$, and $k \in [1, 500]$. The search for a solution starts by substituting sequentially $\rho_{hvi}(k)$ into (20). In this quadratic equation all parameters except ρ_{hvi} are known and there are two solutions for $x(\rho_{hvi})$. Let these two be $x_{1,2}[\rho_{hvi}(k)]$, where square brackets indicate $x_{1,2}$ is a function of $\rho_{hvi}(k)$. Explicitly,

$$x_{1,2}[\rho_{hvi}(k)] = \{-f_a[\rho_{hvi}(k)] \pm \sqrt{f_b^2[\rho_{hvi}(k)] - 4f_a[\rho_{hvi}(k)]c}\}/2f_a[\rho_{hvi}(k)], \quad (22)$$

where the coefficients are

$$f_a[\rho_{hvi}(k)] = \{[A\rho_{hvi}(k)]^2 - A^2\};$$
$$f_b[\rho_{hvi}(k)] = [P_{vM} + P_{hM}A^2 - 2A\rho_{hvi}(k)D_M];$$
$$c = -P_{hM}P_{vM} + D_M^2 + G_M^2.$$

Substitute $x_{1,2}[\rho_{hvi}(k)]$ from (22) into (19) to solve directly for $\{y_{1,2}[\rho_{hvi}(k)]\}^2$, and then substitute $y_{1,2}[\rho_{hvi}(k)]/x_{1,2}[\rho_{hvi}(k)]$ into (21a) so that

$$\rho_{hvi}(k) = 1 - 2y_{1,2}[\rho_{hvi}(k)]/x_{1,2}[\rho_{hvi}(k)]. \quad (23)$$

This equality is imposed by physics, and we proceed to find the specific $\rho_{hvi}(k)$ for which it is valid. Therefore, we search for zero crossing of the functions

$$f[\rho_{hvi}(k)] = 1 - 2y_1[\rho_{hvi}(k)]/x_1[\rho_{hvi}(k)] - \rho_{hvi}(k) \text{ for } k = 1 \text{ to } 500 \quad \text{and} \quad (24a)$$

$$f[\rho_{hvi}(k)] = 1 - 2y_2[\rho_{hvi}(k)]/x_2[\rho_{hvi}(k)] - \rho_{hvi}(k) \text{ for } k = 1 \text{ to } 500. \quad (24b)$$

We name these two "constraining" functions because their zeros are the physical constraints imposed by the melting layer. Furthermore, the two equation in (24) are numerical; hence, the zero crossing does not occur at an integer k but between two ks. At one of these, say k_s, $f[\rho_{hvi}(k_s)] > 0$ and, at $k_s + 1$, $f[\rho_{hvi}(k_s + 1)] < 0$, or it could be vice versa. Regardless of which side of zero crossing we choose, the end result for practical purposes will be same.

It turns out for solution $x_2[\rho_{hvi}(k)]$: $\{x_2[\rho_{hvi}(k)] > P_{hM}\} \wedge \{A^2x_2[\rho_{hvi}(k)] > P_{vM}\}$ violates conservation of power; hence, the opposite inequality must hold. The reason the paradox appears is (17), which cannot distinguish between $\{x_2[\rho_{hvi}(k)] > P_{hM}\} \wedge \{A^2x_2[\rho_{hvi}(k)] > P_{hM}\}$ and $\{P_{hM} > x_2[\rho_{hvi}(k)]\} \wedge \{P_{vM} > A^2x_2[\rho_{hvi}(k)]\}$. Therefore, we retain the pair $x_1[\rho_{hvi}(k)]$, $y_1[\rho_{hvi}(k)]$ satisfying $\{x_1[\rho_{hvi}(k)] < P_{hM}\} \wedge \{A^2x_1[\rho_{hvi}(k)] < P_{vM}\}$ and its corresponding $y_1[\rho_{hvi}(k)]$ from (19). We caution readers that the choice made here is data dependent and must be tested.

We proceed by carrying the pair $x_1[\rho_{hvi}(k)]$, $y_1[\rho_{hvi}(k)]$ and drop $x_2[\rho_{hvi}(k)]$, $y_2[\rho_{hvi}(k)]$. We illustrate next steps with the pair $x_1[\rho_{hvi}(k)]$, $y_1[\rho_{hvi}(k)]$ and take k_s for which zero crossing is between $f[\rho_{hvi}(k_s)]$ and $f[\rho_{hvi}(k_s + 1)]$. Then β from (18a) and (18b) is

$$\beta = \left[\arctan\left(-\frac{G_M}{D_M - Ax_1[\rho_{hvi}(k_s)]}\right)\right] \Big/ 2 + 180°n, \quad n = \pm 1, \pm 2, \ldots, \quad (25)$$

where the principal alias (term preceding $180°n$) $\beta \in [-90°, 90°]$. Therefore, between $-180°$ and $180°$ there are two equally valid solutions for β. From here on we only consider the principal alias.

A very important fact about the ratio $y_1[\rho_{hvi}(k)]/x_1[\rho_{hvi}(k)]$ in (23) is that there are two solutions for $\rho_{hvi}(k_s)$ satisfying $f[\rho_{hvi}(k_s)] = 0$; a physical model in appendix section d confirms this fact. Thus, express the two ratios for which this condition holds as

$$y_{1a}[\rho_{hvi}(k_{sa})]/x_{1a}[\rho_{hvi}(k_{sa})] = [1 - \rho_{hvi}(k_{sa})]/2 \quad \text{and} \quad (26a)$$

$$y_{1b}[\rho_{hvi}(k_{sb})]/x_{1b}[\rho_{hvi}(k_{sb})] = [1 - \rho_{hvi}(k_{sb})]/2, \quad (26b)$$

where the indices "a" and "b" distinguish the two. It is convenient to compact the two ratios to

$$y_{1a}/x_{1a} = [1 - \rho_{hva}]/2 \quad \text{and} \quad (27a)$$

$$y_{1b}/x_{1b} = [1 - \rho_{hvb}]/2, \quad (27b)$$

and through the rest of the paper the smaller of the two intrinsic solutions ρ_{hvi} is ρ_{hvb}. As an aside note that from (15) by substituting x and y into (10) it is possible to compute the transfer gains C_T and C_R.

At this point we suggest a shortcut to compute an approximate β. The simplification replaces $\rho_{hvi}(k_s)$ in (20) with the measured value from the melting layer ρ_{hvM} and then solves for x_1 and evaluates β in (25). This avoids solving for $\rho_{hvi}(k_s)$. In our example ρ_{hvM} is somewhat smaller than ρ_{hvb} and this approximation produced acceptable results (section 4). We warn readers, however, that the approximation may not be universally valid, and in the appendix we have explained and plotted (Fig. A1) the conditions for which the approximation may hold.

FIG. 1. The X-band mobile radar (XERES) at North Base, University of Oklahoma, in Norman.

4. Measurements

We illustrate measurements and results of various computations on an example, then present data solutions from two days.

a. Radar and its data

We made measurements at vertical incidence with the NSSL's 3-cm-wavelength polarimetric radar (Fig. 1) known as X-Pol but nicknamed "XERES" (X-band Experimental Radar for Environmental Studies) after a fictional (invisible) character that drinks Manzanilla Montero in the comic opera *The Gondoliers* by Gilbert and Sullivan (Sullivan 1889). Table 1 lists the radar's characteristics and the pertinent parameters chosen for the experiments in Norman, Oklahoma.

At vertical incidence we rotated the antenna in azimuth and collected 393 radials of data covering 374° (i.e., spacing in azimuth is about 0.95°, so the last 16 radials overlapped the first 16). This we did 14 times ("scans") on 28 April 2021. On closer examination, we dropped the first scan because it was an outlier possibly caused by the system warm-up time. The total duration of the recorded event is about 17 min and consists of 5 scans[1] separated by about 50 s and a 5.5-min gap followed by 9 consecutive scans. On 21 June, we have data from 5 scans but the first was also an outlier; hence, we discarded it.

b. Illustration of the procedure

In the demonstration of the procedure (section 4c) we use primarily data collected on 28 April. The examples in Fig. 2 are vertical cross sections [range–height indicator (RHI)] of the Z, SNR, Z_{DR}, and ρ_{hvM} fields. Noteworthy are large SNRs along the vertical radial.

We took average values of the polarimetric variables (Fig. 3) from each "azimuth" scan and generated the appropriate equations for computing β. The sharp delineation of the bright band is evident in the Z, Φ_{DP}, and ρ_{hvM} extremes at 3.1 km. The peak in $\Phi_{DP} - \Phi_{DPsys}$ is caused by coupling in which β plays a crucial role (12). This can be deduced by noting that the differential phase from rain (5) is $\arg(V^*_{hR}V_{vR}) = \beta + \gamma = \Phi_{DPsys}$. Because in the melting layer $S_{hv} \neq 0$ there is coupling, and (8) yields $\arg(V^*_{hM}V_{vM}) \neq \beta + \gamma$; that is, it differs from Φ_{DPsys}. This difference is due to coupling and enables determining β. The systematic increase in Z_{DR} and decrease in differential phase with height up to 2 km may be system related because these occur in all scans and also in scans from June.

In Fig. 3 we indicate with red lines the standard deviation (SD) of the estimates. For each of the variables the SDs above and below the melting layer are same and depicted to scale with the red lines below the extremes. At the melting layer the SDs are significantly larger because the correlation is lower and SDs depend heavily on ρ^2_{hv} [see Ryzhkov and Zrnić 2019, their (6.76), (6.79), (6.80), and (6.81)]. For clarity we list the pairs of SDs next to each variable: Z (1.8 dB, 1 dB), Z_{DR} (0.75 dB out of scale and therefore not plotted, 0.095 dB), $\Phi_{DP} - \Phi_{DPsys}$ (5.7°, 0.47°), ρ_{hvM} (0.001 very small and therefore not plotted, 0.05).

To check data quality, we plot in Fig. 4a Φ_{DPsys} and in Fig. 4b Z_{DRsys} obtained from pure rain. The blue and black graphs are from the 28 April data at different heights and overlap almost perfectly. The curves are averages from 11 consecutive range locations spaced 37.5 m apart and centered at the indicated heights. Z_{DRsys} is the bias expressed as $-10\log(C^2_R C^2_T) = -20\log(A)$ but written in linear scale in (6). Because these data are from pure rain we expect constant Φ_{DPsys} and Z_{DRsys}. The maximum swing in Φ_{DPsys} is 5° most likely caused by imperfection of the dual

[1] Herein, the scans indicate rotation in azimuth about the beam axis pointed vertically. Subsequently we drop the quotation and imply that the observations are along the same vertical axis.

TABLE 1. Radar parameters.

Wavelength	3 cm
Polarimetric mode	Simultaneous H, V transmission and reception
Scanning capability	In azimuth and elevation
Peak transmitter power	200 kW
Beamwidth	1°
Pulse width	0.25 μs (for the experiment); variable up to 2 μs
Spacing in range	0.25 μs (37.5 m) during the experiment
Max range	20 km (for the experiment)
No. of samples in range	541
Sample spacing in range	37.5 m (for the experiment); variable up to about 150 m
Pulse repetition frequency	949.9934 Hz (for the experiment); variable otherwise
Transmission modes	Uniform sequences at variable PRT
No. of samples for computing the polarimetric variables, M	128 (for the experiment); variable otherwise
Antenna rotation rate	About 7.52° s^{-1}
Spacing in azimuth	About 1°

rotary joint. Z_{DRsys} variations may also be caused by the rotary joint. However, the swing of about 0.015 dB is negligible. Examination of similar data from 21 June 2021 reveals almost exact match in Φ_{DPsys} with azimuth (Fig. 4a, red graph) strengthening the hypothesis that the cause is stable and system related. The trends in Z_{DRsys} are similar, having an offset slightly less than 0.1 dB and a hint of a first harmonic over the 360° interval. Gorgucci et al. (1999) attribute observation of periodic Z_{DR} (10 cm wavelength) at vertical incidence to contamination by ground clutter. They cite a peak to peak excursion of 0.3 dB. Our observation at the 3 cm wavelength had no clutter contamination at the heights we use for measurements and peak to peak swing is about 0.02 dB (Fig. 4b). Because subsequently we average data over about 360° the effects of periodic variations vanish.

Next we illustrate computation of β. First, we identify a range interval in rain where the vertical profiles of the

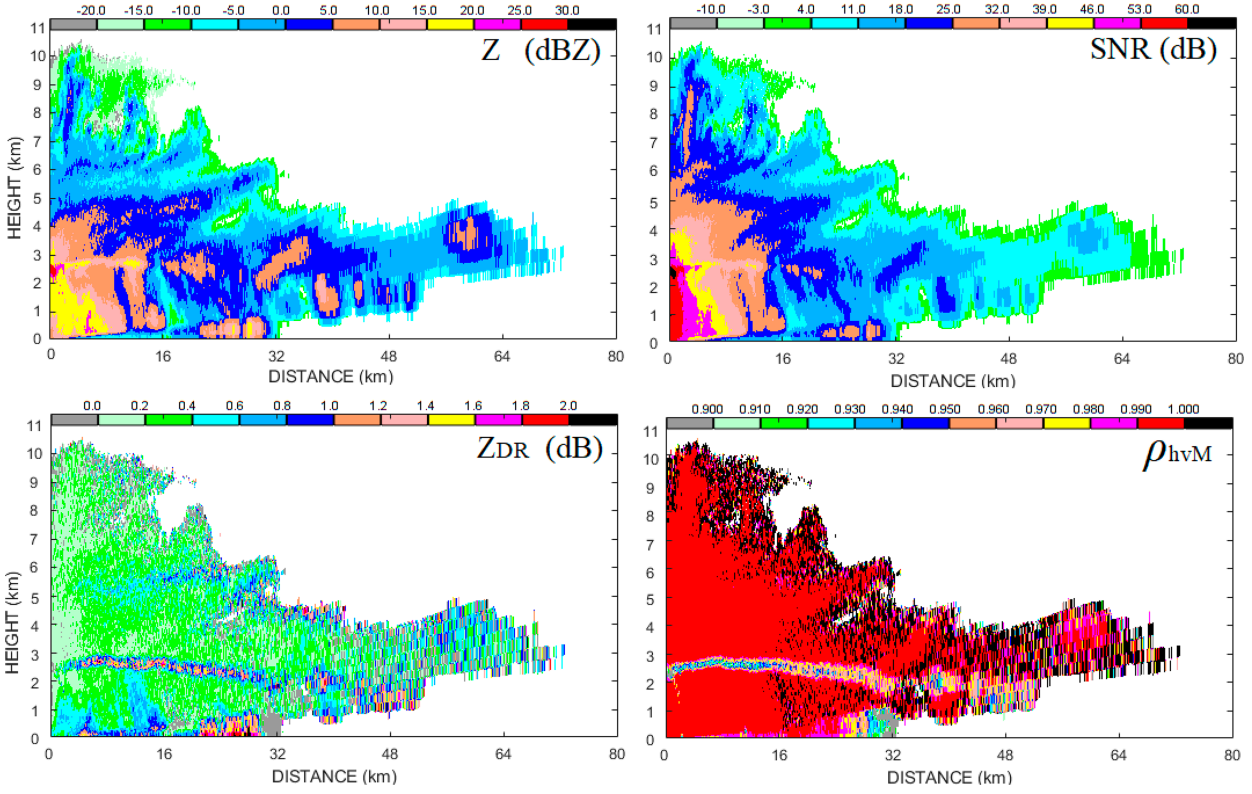

FIG. 2. Vertical cross sections of (top left) reflectivity, (top right) signal-to-noise ratio, (bottom left) differential reflectivity, and (bottom right) correlation coefficient. The subscript M indicates measured by radar everywhere (in addition to the melting layer) although in rain ρ_{hvM} most likely is equal to ρ_{hvi}. The scan is an RHI from 0° to 90°. The date is 28 Apr 2021.

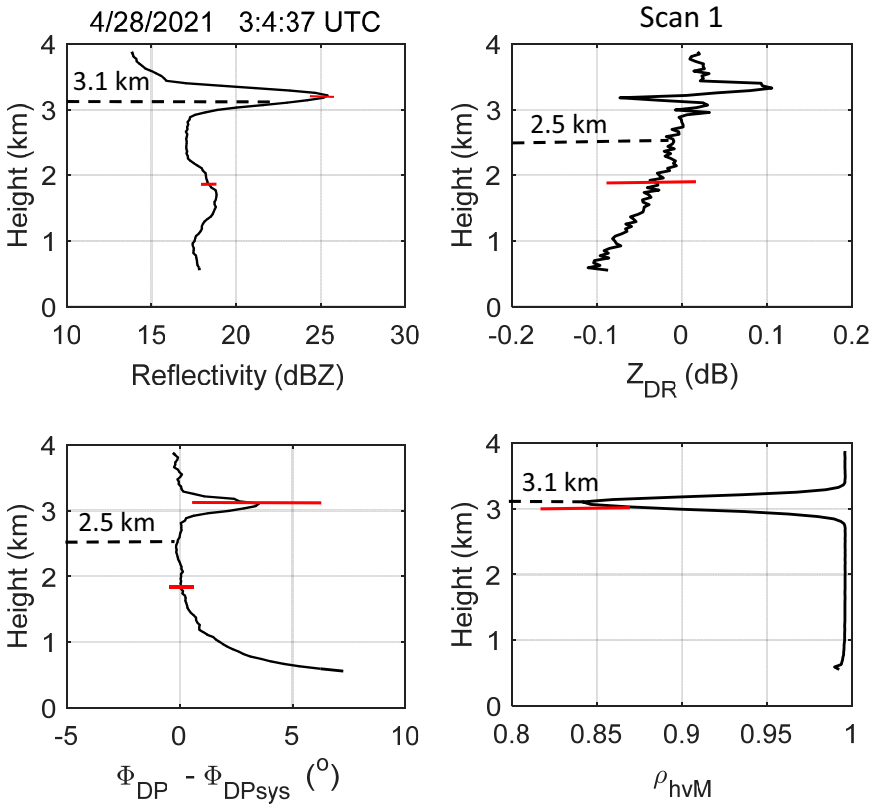

FIG. 3. Vertical profiles of the polarimetric variables. The data are averages from 393 consecutive positions in azimuth. The system differential phase in this case was determined from data at 2.5 km (dashed line in the plots of Z_{DR} and $\Phi_{DP} - \Phi_{DPsys}$), and its value 36.8° we subtracted from the measured differential phase and plotted in this figure. The melting layer at 3.1 km is well depicted by the minimum in $\rho_{hvM} = 0.842$. The red lines indicate the standard deviation of the variables. The date is 28 Apr 2021.

polarimetric variables are locally constant. In Fig. 3 this is between 2.3 and 2.9 km. We choose the 2.5 km height (dashed lines in Z_{DR} and $\Phi_{DP} - \Phi_{DPsys}$ plots) to determine Φ_{DPsys} (from the argument of the cross correlation in rain R_{hvR}) and bias (6) in Z_{DR}. We removed $\Phi_{DPsys} = 36.8°$ from the plot (Fig. 3).

We determined the height of minimum ρ_{hvM} (Fig. 3, dashed line) to be 3.1 km and its value $\rho_{hvM} = 0.842$. We computed

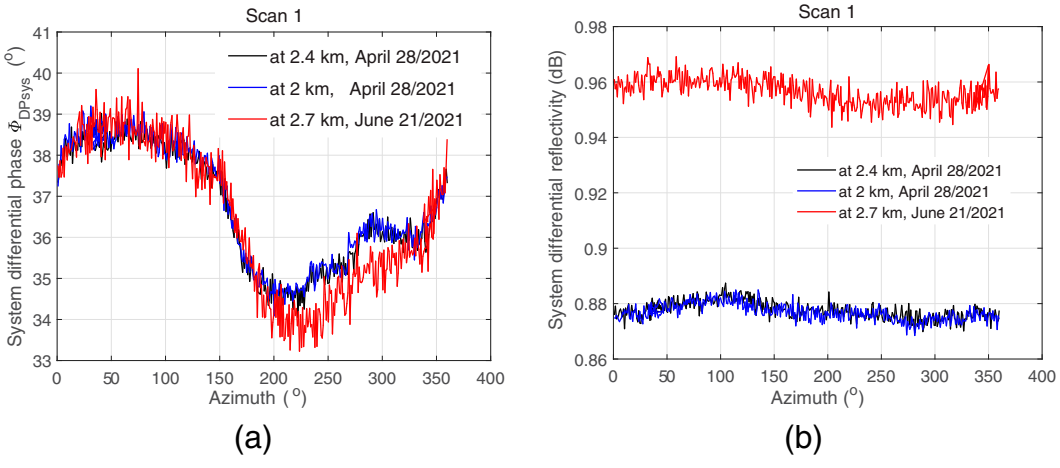

FIG. 4. (a) Dependence of the system differential phase on azimuth. (b) Dependence of system differential reflectivity on azimuth. Each curve is an average of 11 consecutive values in range. The location of the center of the range is indicated in the legend. The dates are 28 Apr and 21 Jun 2021.

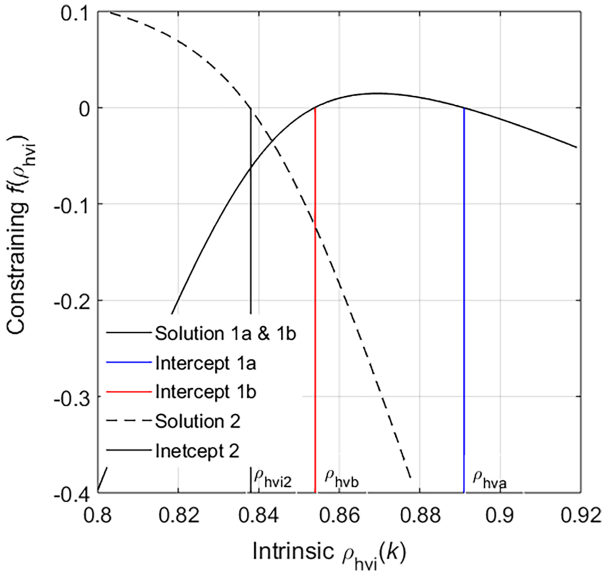

FIG. 5. The functions $f(\rho_{hvi})$ [(24)] depicting the difference between the postulated relation (23) and the intrinsic correlation coefficient $\rho_{hvi}(k)$, scan 1. The intersection of the dashed curve and the zero line is the solution 2 from (24b), indicated with ρ_{hvi2}. It occurs at ρ_{hvi} of 0.838 (intercept 2), produces a copolar power larger than the sum of copolar and cross-polar power, and hence is physically forbidden. The other two b intercept lines are positioned at the zero crossing occurring where $\rho_{hva}(391) = 0.891$ (intercept 1a) and $\rho_{hvb}(354) = 0.854$ (intercept 1b).

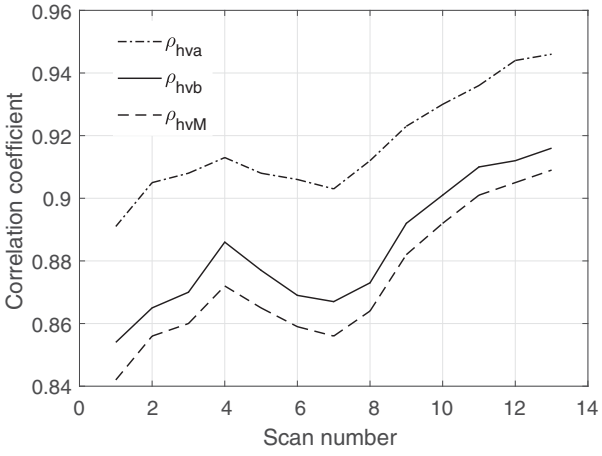

FIG. 6. Measured and intrinsic correlation coefficients (the minima in the melting layer) obtained from 13 scans. Data are from 28 Apr 2021.

P_{hM}, P_{vM}, and R_{hvM} from that height (the dashed line in reflectivity plot indicates the height from which the two powers originate and the dashed line in ρ_{hvM} plot indicates where R_{hvM} originates) and substituted in (10)–(13). Then following the described procedure (section 2a), we construct (20) and write two solutions for x in (22). We find from (22) the specific x_1 corresponding to $\rho_{hvi}(k_{s1})$ and x_2 corresponding to $\rho_{hvi}(k_{s2})$. In our case $x_2 > P_{hM}$ and is dismissed because it contradicts $P_{hM} = x_2 + C_T^2 y_2$ in (10a). Therefore, we accept x_1 and proceed to solve for β.

It turns out there are two distinct ρ_{hvi}s, each producing a valid pair x_1, y_1 (27); ρ_{hva} corresponds to x_{1a}, y_{1a}, and ρ_{hvb} corresponds to x_{1b}, y_{1b} (Fig. 5). In the appendix, we prove using a model of the melting layer that in our case the pair x_{1b}, y_{1b} is correct. The model consists of closed form solutions for the statistical intrinsic backscattering properties enabling computation of the radar variables in the SHV polarimetric mode. Varying β and applying our retrieval procedure, we obtain two relations $\beta_a(\beta)$ and $\beta_b(\beta)$ having different slopes. Most importantly in one range of β, $d\beta_a/d\beta > d\beta_b/d\beta$ and in the complement range $d\beta_b/d\beta > d\beta_a/d\beta$. Identical inequalities for the slopes of $dx_{1a}/d\beta$ and $dx_{1b}/d\beta$ hold. Thus, from the test of the latter two slopes on data we determined the correct β within the interval from $-90°$ to $0°$.

Having identified that solution 1b is valid, we proceed to determine ρ_{hvi}: hence plot (Fig. 5) $f[\rho_{hvi}(k)]$ versus $\rho_{hvi}(k)$ as stipulated by (24b). Recall per (15a) and (15b) that $x = C^2\langle|S_{hh}|^2\rangle$ and $y = C^2\langle|S_{hv}|^2\rangle$ are functions of ρ_{hvi} that we have expressed as solutions (22) and (23). There are two zero crossings of $f[\rho_{hvi}(k)]$, one at the intrinsic $\rho_{hvb}(k_s) = 0.854$ (at $k_s = 354$) and the other at $\rho_{hva}(k_s) = 0.891$ (at $k_s = 391$) (Fig. 5); upon substituting into (25) we find two solutions for β: $\beta_a = -47.6°$ and $\beta_b = -24.7°$. In the appendix section d, we show how to determine which of the two solutions is valid, and, in our case, $\beta_b = -24.7°$ is the correct one and so is its alias $\beta_b' = \beta_b + 180^o = 155.3^o$. Note that the alias indicates the polarization is orthogonal. Therefore, our method cannot determine if the transmitted polarization is left-hand elliptical or orthogonal right-hand elliptical. Either polarization is equally depolarized by precipitation; hence, depolarization ratios are same. Clearly, diagnosing and/or quantifying precipitation using depolarization ratios would not be affected. Henceforth, we consider only the negative solution β_b. We have analyzed data from all scans and found relatively tight cluster of β_b estimates and credible ρ_{hvb} values. Before dwelling on these results we present comparison of computed (intrinsic) ρ_{hva} and ρ_{hvb} with the measured ρ_{hvM} for 13 scans (Fig. 6).

The plots of ρ_{hvb} and ρ_{hvM} in Fig. 6 are very similar. The values are close to each other and at every point $\rho_{hvM} < \rho_{hvb} < \rho_{hva}$. This consistency is expected from physical principles rooted in coupling as the following heuristic argument explains. In the expression for computing correlation coefficients (i.e., $\langle V_h^* V_v\rangle$), the portion of V_h signal coupled to V_v signal is perfectly correlated with the original V_h signal, and vice versa. If coupling is positive this would increase the correlation coefficient ρ_{hvM}. Otherwise, it would decrease it as is the case here. Therefore, we submit the coupled component is out of phase with respect to the main signal. Moreover, the closeness of ρ_{hvM} and ρ_{hvb} suggests that the intermediate determination of ρ_{hvi} for estimating β might not be needed. It may suffice to replace ρ_{hvi} in (20) with ρ_{hvM} and solve for β. We stress that this is not a universal principle but is specific for the β on our radar. Further explanation is in the appendix following (A9) and in Fig. A1.

The measured Φ_{DPsys} from the 13 scans is in Fig. 7a, and the retrieved β is in Fig. 7b. The time between the first and

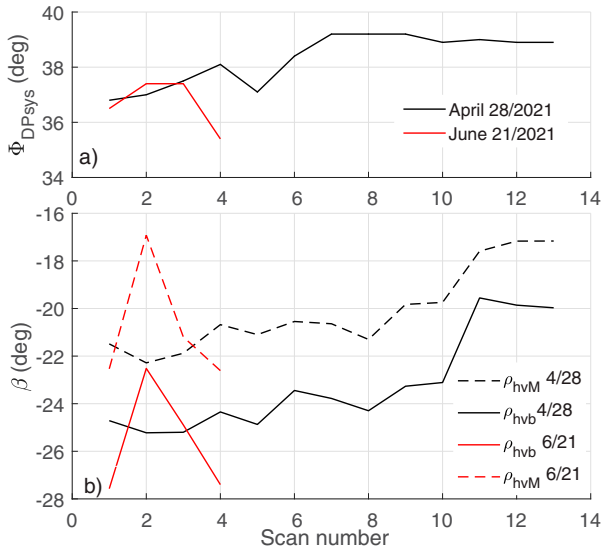

FIG. 7. (a) System differential phase dependence on the scan number. (b) Transmitted differential phase dependence on the scan number. The plotted differential phases are $\beta(\rho_{hvb})$ obtained using intrinsic correlation coefficient and $\beta(\rho_{hvM})$ using the measured correlation coefficient.

fourth scans (April) is about 3.5 min. A 5.5-min gap follows after which a regular separation by about 50 s resumes. We speculate that the gradual rise of Φ_{DPsys} over the first four scans may be due to transient features of the system, like warming up of various components. The similar rise from the fifth to seventh scan may also be transient because after the fourth scan radar operation changed to collect some RHI and PPI data. Then we changed back the radar parameters and that is where the fifth scan started. Φ_{DPsys} during the last time segment has settled to about 39° suggesting steady state.

We include in Fig. 7 the result from four scans made on 21 June 2021 when the melting layer was at 3.9 km and the reflectivity profile (Fig. 8) had values about 12 dB smaller than in the April case (Fig. 3). The times between scans 1, 2, 3, 4 are 6 min, 30 s, and 22 min. Note (Fig. 7) the consistency of both Φ_{DPsys} and β between the April and June data. The exact β (computed from ρ_{hvb}) changes within 5°; the one from ρ_{hvM} is also within 5° but positively offset by about 4°. The values from the second case are not affected by the 12 dB decrease of Z (SNR loss of about 14.8 dB) in the melting layer on 21 June.

The change of β computed from ρ_{hvb} on both days is within about 8°. This is acceptable for gauging biases in polarimetric variables or computing elliptical depolarization ratios as the following argument suggests. Assume that the error in β is 10° and that the intended polarization is circular [(4)], implying $\beta = 90°$. Take a representative value of the linear depolarization ratio $L_{dr} = 0.01$ (i.e., −20 dB in logarithmic scale) and a $\rho_{hvi} = 0.86$ as in Fig. 6 for a well-developed melting layer. Also let (9a) and (9b) hold. Then substituting these values in (3) for $\beta = 90°$ produces the EDR = 0.0860 (true CDR) and doing the same but for $\beta = 100°$ produces erroneous CDR; that is, EDR = 0.0857. The error is about 0.35% and is deemed insignificant.

c. Sensitivity

The retrieved β depends on estimates of Φ_{DPsys} in rain and ρ_{hvM} in the melting layer. Averaging data over a full circle reduces the standard errors of the β estimate but does not eliminate bias. Here we examine bias by varying the measured Φ_{DPsys} and the ρ_{hvb} from the 28 April data. Thus, we took the thirteenth scan to illustrate sensitivity to system differential phase and varied Φ_{DPsys} about the measured values of 39° but kept everything else same (Fig. 9a). The change $\Delta = \hat{\Phi}_{DPSys} - 39°$ by ±1° (centered on 0° indicated with an open circle) causes a −7° or +12° change in β. Thus, the small change in Φ_{DP} causes a significant change in β and is the reason to average over the full circle and rotate slowly the antenna (1.25 rpm). That way there is a sufficient number of samples per radial (128; Table 1) to reduce statistical uncertainty. Sensitivity to ρ_{hvM} we estimated from the same scan by varying it while keeping $\Phi_{DPsys} = 39°$. Variation of ρ_{hvM} encompasses our computed 0.84–0.95 collective range of all three correlations (Fig. 6). In this scan $\rho_{hvM} = 0.916$ and the variation between 0.906 and 0.926 (0.02 net increase) causes a variation in β between −16° and −25° (Fig. 9b). For practical purposes this uncertainty may be acceptable considering the large change in ρ_{hvM}. As seen from the slope (Fig. 9b), sensitivity decreases with decreasing ρ_{hvM}. This favors measurements in well-developed melting layer where ρ_{hvM} is low like, for example, 0.8 as reported by Zrnić et al. (1994a). Clearly the retrieved β is not very sensitive to ρ_{hvM} but is moderately sensitive to Φ_{DPsys}.

d. Other variables and height of the melting layer

For completeness we present the height of the melting layer determined by the minimum in ρ_{hvM} (Fig. 10a) and the values of the minimum (Fig. 10b) for each radial of the April scan 1. The time separation of data (radials) is 135 ms, and the total time to accomplish one scan is about 50 s. The graphs have quick variations attributable to statistics of processing and slow variations likely caused by the radar system and possibly by temporal variation in the signals characteristics.

Z at the melting layer and its height as function of the scan number are in Fig. 11a. The almost constant Z from scan 1 to about 8 implies presence of stratiform precipitation in steady state. It is followed by a decrease indicating waning precipitation. Toward the end of the event the correlation coefficients increase (Fig. 6) likely because the strength Z of the melting layer decreases (Fig. 11a) as snowflakes are smaller and less numerous. We expect that smaller scatterers would have larger ρ_{hvi} because their shapes are less rugged. The small sizes prevail at the end of the precipitation process, possibly because of size sorting. Larger aggregates fall out scavenging or leaving smaller ones behind; the rise of the melting layer is about 135 m between the 7th and 12th scan (about 4-min time separation).

The graphs of the linear depolarization ratio as computed via (21b) from

$$L_{DRM} = 10 \log[(1 - \rho_{hvM})/2], \tag{28}$$

which uses the measured ρ_{hvM}, and the intrinsic one from

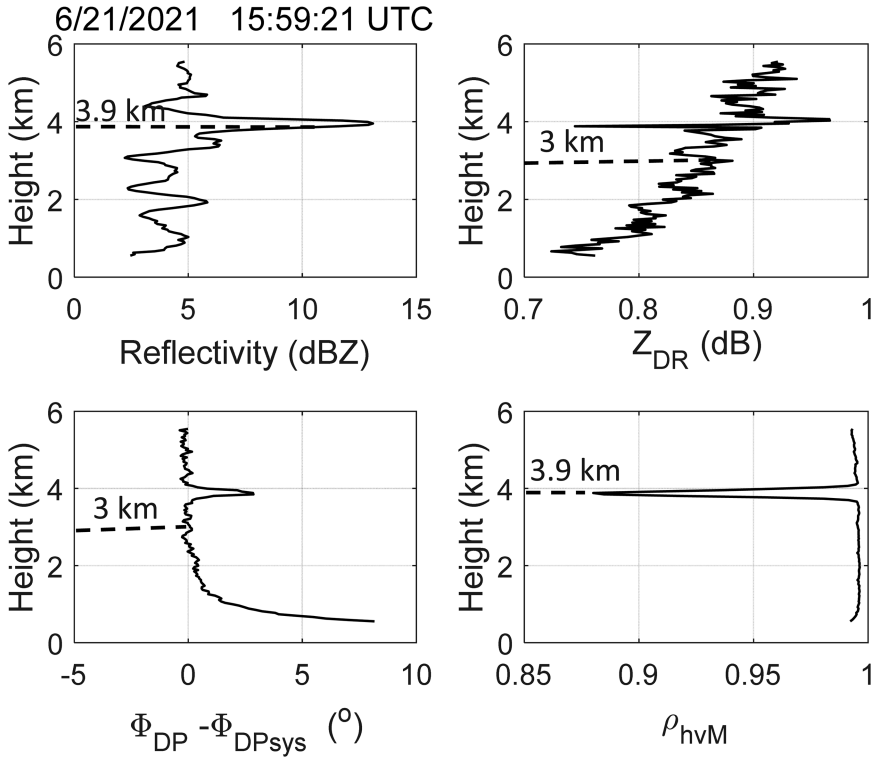

FIG. 8. As in Fig. 3, but the data are from 21 Jun 2021, scan 1. The system differential phase we estimate from rain at 3 km to be 36.7°.

$$L_{\mathrm{DR}b} = 10\log[(1-\rho_{\mathrm{hv}b})/2] \tag{29}$$

follow each other closely (Fig. 11b). The values agree well with the observation by Zrnić et al. (1994b), whose maximum L_{DR} of −10 dB was measured at vertical incidence with another 3-cm-wavelength radar in Florida.

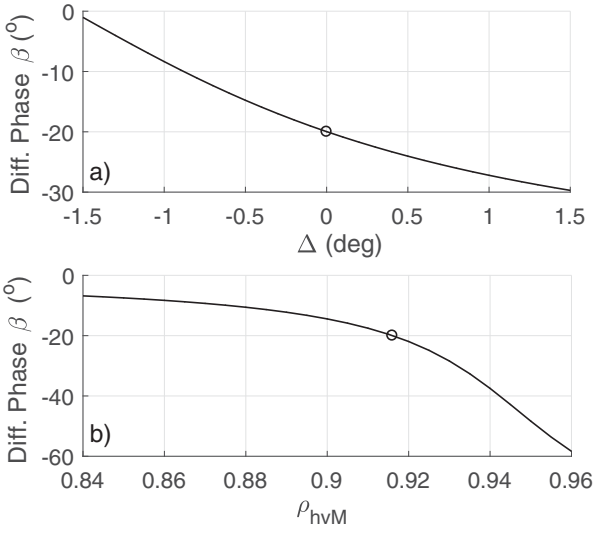

FIG. 9. (a) Sensitivity of differential phase estimate β, to the error in the estimate of the system differential phase Φ_{DPsys}. (b) Sensitivity of β to the measured correlation coefficient. The open circle indicates the measured value, and the curves are the deviations about it.

Although our results are self-consistent and statistically stable, we do not have independent engineering measurements of transmitter differential phase. We have compared an engineering measurement on a University of Oklahoma radar with the β estimate from one partial scan (110° rotation) at vertical incidence. On that radar it is possible to inject a phase difference between the H and V transmitted signals. Then, at a few hundred meters from the radar, receive the sum of the two signals and back out the initial β. The value thus measured was acceptable but not sufficient to validate our method.

5. Summary

We presented a method for estimating β from measurements of ρ_{hvM} in a melting layer and simultaneous Φ_{DPsys} in rain below. It is rooted in physical principles of which the relation (21a) between $\rho_{\mathrm{hv}i}$ and L_{dr} is very important. This relation is valid for snowflakes randomly oriented in the horizontal (polarization) plane as expected at vertical incidence in the melting layer.

The theory involves forming a quadratic equation for $x = C^2\langle|S_{\mathrm{hh}}|^2\rangle$ from three coupled nonlinear equations. One of the two solutions, labeled 2 (i.e., x_2) does not conserve power because it is larger than the total returned power P_{hM}; it is therefore discarded, and solution 1 (x_1) is further

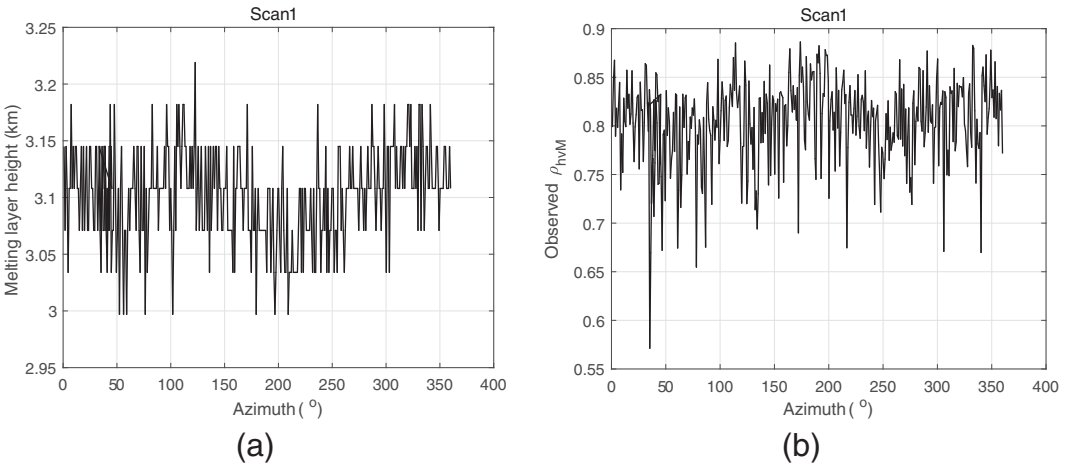

FIG. 10. (a) Height of the melting layer at the location of ρ_{hvM} vs azimuth. (b) Observed values of min(ρ_{hvM}) vs azimuth. The date is 28 Apr 2021, scan 1.

processed. It turns out that the coefficients of the quadratic equation are nonlinearly related to the intrinsic correlation ρ_{hvi}. Therefore, we resorted to a numerical solution yielding two intrinsic coefficients ρ_{hva} and ρ_{hvb}; throughout the paper ρ_{hvb} is the smaller of the two. The two correlation coefficients correspond to two β estimates and the signs of these estimates we determine from the signs of the measured correlation function. In our case matching signs reveals the principal alias of β is negative and with this knowledge we constrain search to between $-90°$ and $0°$. To find β, we developed in the appendix a model of the melting layer.

The valid β solution has a twin (alias) offset by 180° and there is no way to find which of the two is correct. The twin solution corresponds to the orthogonal polarization and therefore is not detrimental for applications needing β. This is because the elliptical depolarization ratio is same for both solutions and so are effects on the bias of polarimetric variables.

We have determined average β of the April case to be either $-23°$ or 157°. Thus, XERES transmits elliptically polarized waves that can be represented with either ellipse in Fig. 12. To plot these, we have set to one the amplitude ratio C_T between the two transmitted components. Our method can separate the differential bias (in voltage equivalent) on transmission C_T from the one on reception C_R. And in all scans except the last two the C_T was between 0.96 and 1.11. Values close to one are expected as the following argument explains. In the SHV mode the transmitter power is split evenly between two waveguides, one for H, the other for V polarization. The split powers are recombined by an orthomode coupler connected to the antenna feed. These microwave components are passive and very stable. Therefore, the transmitted wave has almost equal magnitude of its H and V components. The polarization is elliptical with ellipse orientation either $-45°$ or 45°. Because the ellipticity angle $\chi = |\beta_b|/2 = 11.5°$, the minor-to-major-axis ratio tan(χ) is 0.235.

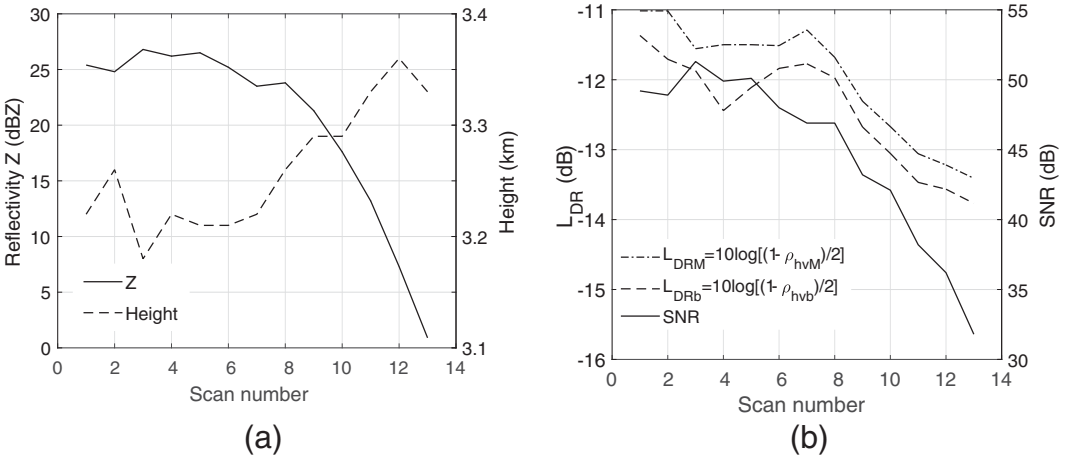

FIG. 11. (a) Reflectivity and the height of the melting layer for the 28 Apr case. (b) Signal-to-noise ratio (SNR) and linear depolarization ratios L_{DR} (dB). The date is 28 Apr.

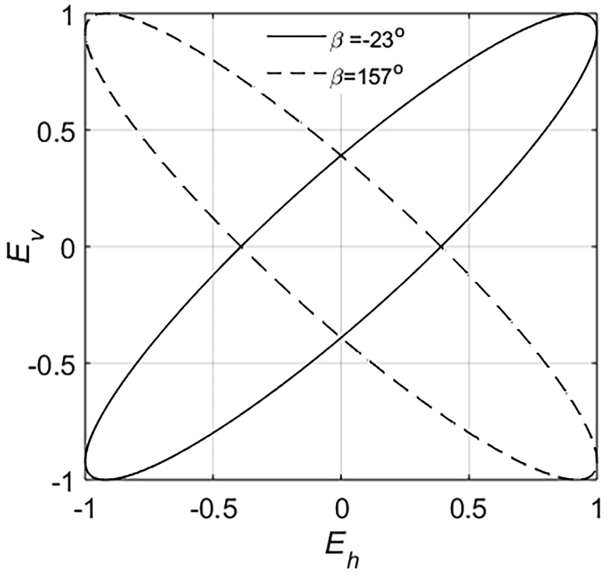

FIG. 12. Two possible polarization states of waves transmitted by XERES. The ellipse having the longer axis at 45° has $\beta = -23°$ and indicates right-hand polarization. The other ellipse is for $\beta = 157°$ and indicates left-hand polarization. The two polarizations are orthogonal to each other. The ambiguity is inherent to the measurement, and the magnitudes of the E_h and E_v fields are set to 1.

There is one more characteristic of the XERES that can be deduced from our analysis, and it is the receiver differential phase. The average system differential phase during the April experiment was 38°. From the 13 scans the average β is −23°. Consequently, we deduce that the receiver differential phase $\gamma = 38° + 23° = 61°$. Moreover, we can compute the correlation coefficient between β and Φ_{DPsys}. It is 0.58 signifying that some variability of β is partially responsible for the variability in Φ_{DPsys}. The sample variance of β is $4.2^{\circ 2}$ whereas Φ_{DPsys} sample variance is $0.22^{\circ 2}$. We submit the difference is caused by the physics of measurements. Φ_{DPsys} we estimate from returns in rain. These are much more stable than the ones from the melting layer. We chose locations in rain where the differential phase is locally uniform over about 500-m-wide height interval. The returns from the melting layer originate at the minimum of ρ_{hvM} where considerable variation of the signal attributes (like powers and correlation) exists. Moreover, the variances increase significantly at smaller values of ρ_{hv}. Further, for estimating β we use five variables (P_{hM}, P_{vM}, R_{hvM}, Φ_{DPsys}, and Φ_{DP}). If variances of these were comparable to the one of Φ_{DPsys}, and the variables were independent the sum of the variances would about equal to the variance of β.

Last, we have automated most of the procedure with some exceptions as follows. We manually determine Φ_{DPsys} by plotting vertical profile of Φ_{DP} and then subtracting (in the program) a test Φ_{DPsys} a few times until the straight part of $\Phi_{DP} - \Phi_{DPsys}$ aligns with the zero line. The value of ρ_{hvM} we determine automatically, but for three scans we took the ρ_{hvM} from a range gate above the one where the minimum occurred. Otherwise some of the computations produced physically meaningless results like a negative discriminant. In our experiment the range gate's spacing was 37.5 m; hence, data from one sample above the minimum ρ_{hvM} were well within the melting layer.

6. Conclusions

We have developed a measurement procedure to determine the differential phase on transmission, β between two orthogonal linearly polarized fields in the SHV polarimetric mode. This measurement we demonstrated on the NSSL's X-band polarimetric radar (nicknamed XERES). Determining β is possible because coupling causes deviation of the observed differential phase from the system differential phase at vertical incidence in the melting layer. Coupling through rain at vertical incidence is negligible enabling us to determine the system differential phase and bias in differential reflectivity.

It is crucial that the precipitation has a melting layer. During measurements the vertically pointing antenna rotates about its axis so that upon completion of one cycle there are over 360 radials of data. This large number of observations reduces statistical variation in estimates of polarimetric variables. We use returns from the melting layer at the minimum of the measured correlation coefficient ρ_{hvM} to compute powers and cross correlation. These and the theoretical relation between the intrinsic correlation coefficient ρ_{hvi} and the linear depolarization ratio form a set of nonlinear equations in which β is one of the variables. We have solved this set by a hybrid method. It consists of an analytic solution to a quadratic equation in $x = C^2\langle|S_{hh}|^2\rangle$ where ρ_{hvi} is a free parameter. The constraint on power conservation (measured reflectivity at horizontal polarization must be larger than intrinsic reflectivity) enables resolving one ambiguity revealing the path to the correct solution. Changing ρ_{hvi} uncovered one more ambiguity in ρ_{hvi} that must be dealt with. The two ambiguous values are ρ_{hva} and ρ_{hvb}. The ambiguous pair ρ_{hva}, ρ_{hvb} produces a pair β_a, β_b needing resolution. For this we use slopes of functions $\beta_a(\beta)$, $\beta_b(\beta)$. These are uniquely related to slopes of the other polarimetric variables like $x(\beta)$ and that is sufficient to identify the correct β.

In our case the correct one is β_b. Nonetheless, β_b is indistinguishable from its twin, offset by 180°. Both are equally acceptable. This is because the underlining principal unambiguous interval, 360° applies to $2\beta_b$. The elliptical depolarization ratio computed using β is the same for the RHE (corresponding to negative β) and the LHE (corresponding to $\beta + 180°$); polarization senses are opposite if $\beta > 0$. The two cross-polar ratios carry the same information about scatterers. We have determined that XERES transmits elliptically polarized waves with minor-to-major-axis ratio (ellipticity) of about 0.2 and orientation very close to −45° or 45°. This solution is stable over the duration of the experiment with a variation of few degrees and is very close to the solution from a dataset obtained two months later.

We show that in the case of the melting layer at vertical incidence computing β can be simplified by using the measured correlation coefficient in lieu of the intrinsic one. Herein, the difference between the exact results and the approximate ones is about −4° and is deemed sufficiently small for most applications. It is also important that in this approximation

the procedure does not depend on the differential reflectivity bias. Nonetheless it required knowledge of the system differential phase. We caution readers that this approximate solution is not universally valid but holds for a range of β and we have shown how to find this range.

A by-product of the computation is the linear depolarization ratio in the melting layer. Its range of values agrees reasonably well with observations by others. However, at vertical incidence the L_{DR} is redundant as it is uniquely related to the intrinsic $\rho_{\mathrm{hv}i}$. The measured ρ_{hvM} and the intrinsic $\rho_{\mathrm{hv}i}$ follow each other closely, and in our data ρ_{hvM} is smaller than $\rho_{\mathrm{hv}i}$.

Knowledge of the system differential phases β and γ (of the receiver) takes guesses and approximations out of the depolarization ratios computation. This might enable better matching of observations with model calculations and ultimately should improve classification of hydrometeors. It may produce more precise classification and possibly quantification of snow crystals, for example, from the elevation angle dependencies of the depolarization ratios. Even hail sizing may benefit from differential phase measurements.

Our methodology cannot be applied directly to the WSR-88Ds because the maximum elevation angle on these radars is structurally limited to 60°. Therefore, an in-depth study on how to determine β from data on radars with no vertical pointing capability is in order. If successful it would enable estimating cross-polar power, or linear depolarization ratio. These variables are generally independent of other polarimetric variables and therefore would bring a new piece of information onto the table.

Acknowledgments. Workers D. Wasielewski, M. Shattuck, and C. Smith maintained the XERES radar and assisted in experimental setup. The comments of A. Ryzhkov, L. Hooper, and S. Matrosov have improved comprehension of the paper. Author V. Melnikov was supported by NOAA/Office of Oceanic and Atmospheric Research under NOAA–University of Oklahoma Cooperative Agreement NA21OAR4320204, U.S. Department of Commerce. Three anonymous reviewers gave us penetrating comments, uncovered some errors, and improved considerably this paper.

Data availability statement. Data used in this study are stored in the NSSL archive and can be obtained from NSSL or the authors.

APPENDIX

Relations and Assumptions

Various relations underpinning the assumptions and depolarization ratios are briefly reviewed/derived. Moreover, we use an analytic model to arrive at the correct solution for β. Throughout we assume the SHV polarimetric mode.

a. Relations between the backscatter matrix elements and radar voltages

The relation between voltages generating the transmitted fields and the received voltages $|V_{\mathrm{h}}\ V_{\mathrm{v}}|^{\mathrm{T}}$ (T signifies transpose) corresponding to the backscattered fields is expressed as [from Ryzhkov et al. 2017, their (2)]

$$\begin{vmatrix} V_{\mathrm{h}} \\ V_{\mathrm{v}} \end{vmatrix} = C \begin{vmatrix} 1 & 0 \\ 0 & C_R e^{j\gamma} \end{vmatrix} \begin{vmatrix} e^{-j\Phi_{\mathrm{DP}}/2} & 0 \\ 0 & 1 \end{vmatrix} \begin{vmatrix} S_{\mathrm{hh}} & S_{\mathrm{hv}} \\ S_{\mathrm{vh}} & S_{\mathrm{vv}} \end{vmatrix} \begin{vmatrix} e^{-j\Phi_{\mathrm{DP}}/2} & 0 \\ 0 & 1 \end{vmatrix} \begin{vmatrix} 1 \\ C_T e^{j\beta} \end{vmatrix}, \tag{A1}$$

where the second subscript on the elements of the backscattering matrix indicates the polarization of the incident field and the first subscript indicates the polarization of the backscattered field. The C contains the radar constant, dependence on range, range weighting function, and other parameters so that the units on the right side are volts (consistent with the left side), and it relates measurements of powers and correlations to the second-order moments such as $\langle|S_{\mathrm{hh}}|^2\rangle$ or $\langle|S_{\mathrm{vv}}|^2\rangle$ or $\langle S_{\mathrm{hv}}^* S_{\mathrm{hh}}\rangle$ and so on containing precipitation properties [see Ryzhkov and Zrnić 2019, their (3.10), (3.13), and others]. Equation (A1) indicates that on transmission a unit voltage generates the incident fields $E_{\mathrm{h}}^i \propto 1$ and $E_{\mathrm{v}}^i \propto C_T e^{j\beta}$; hence, $\beta = \arg(E_{\mathrm{h}}^{i*} E_{\mathrm{v}}^i)$. The imbalance in amplitude between the two transmitted fields is $|E_{\mathrm{v}}^i/E_{\mathrm{h}}^i| = C_T$. The C_R is the amplitude imbalance caused by the receiver, and γ is the receiver's differential phase. [Our convention stipulates opposite signs of transmitter and receiver differential phases from the one in Ryzhkov et al. (2017).] For reciprocal scatterers like hydrometeors the diagonal terms of the backscattering matrix are equal; that is, $S_{\mathrm{hv}} = S_{\mathrm{vh}}$. The differential phase due to two-way propagation is Φ_{DP}, and at vertical incidence it is zero. Therefore, we replace the transmission matrix (the 2×2 matrix second and fourth from the right) with the identity matrix so (A1) becomes

$$\begin{vmatrix} V_{\mathrm{h}} \\ V_{\mathrm{v}} \end{vmatrix} = C \begin{vmatrix} 1 & 0 \\ 0 & C_R e^{j\gamma} \end{vmatrix} \begin{vmatrix} S_{\mathrm{hh}} & S_{\mathrm{hv}} \\ S_{\mathrm{hv}} & S_{\mathrm{vv}} \end{vmatrix} \begin{vmatrix} 1 \\ C_T e^{j\beta} \end{vmatrix}. \tag{A2}$$

Evaluation shows that the return to the antenna's port for horizontal polarization is $C(S_{\mathrm{hh}} + S_{\mathrm{hv}} C_T e^{j\beta})$. The second term means the vertically transmitted field couples via S_{hv} to the horizontally backscattered component.

b. Relations for rain

The raindrop shape is well represented by horizontally oriented oblate spheroids. Hence, the shape in the horizontal plane (the polarization plane at vertical incidence) is circular. Note that at vertical incidence polarization labels H and V serve only to indicate that the two fields are orthogonal. The orientation of the antenna in azimuth determines the absolute direction of the two fields. Symmetry requires that $\langle|S_{\mathrm{hh}}|^2\rangle = \langle|S_{\mathrm{vv}}|^2\rangle$ and also $S_{\mathrm{hv}} = S_{\mathrm{vh}} = 0$. However, if raindrops change shape in the polarization plane, for example, by oscillating, the cross-polar term $\langle|S_{\mathrm{hv}}|^2\rangle$ may not be zero but would be significantly smaller than the copolar one. Moreover, if the drops symmetry axis deviates from the vertical (drops are canted) $\langle|S_{\mathrm{hv}}|^2\rangle$ is not zero. Rotating antenna and averaging the measurements would eliminate these geometric effects on estimates of Z_{DR}. Introducing the listed conditions for rain reduces (A2) to

$$\begin{vmatrix} V_{hR} \\ V_{vR} \end{vmatrix} = C \begin{vmatrix} 1 & 0 \\ 0 & C_R e^{j\gamma} \end{vmatrix} \begin{vmatrix} S_{hh} & 0 \\ 0 & S_{vv} \end{vmatrix} \begin{vmatrix} 1 \\ C_T e^{j\beta} \end{vmatrix} = C \begin{vmatrix} S_{hh} \\ C_R C_T e^{j(\beta+\gamma)} S_{vv} \end{vmatrix}. \tag{A3}$$

c. Relations for melting layer

Randomly oriented prolate spheroids with symmetry axis (of length a) in the horizontal (polarization) plane capture the essential backscattering properties of wet snowflakes. We use results from Bringi and Chandrasekar (2001) to construct relations between the various second-order moments of the backscattering matrix elements. Specifically, we adapt their (2.53a), (2.53b), and (2.53c). In the backscattering alignment convention, these equations are

$$S_{hh} = K[\alpha + (\alpha_{zb} - \alpha)\sin^2\theta_b \sin^2\phi_b], \tag{A4a}$$

$$S_{hv} = K\Big[\frac{(\alpha_{zb} - \alpha)}{2}(\cos\theta_i \sin^2\theta_b \sin 2\phi_b + \sin\theta_i \sin 2\theta_b \sin\phi_b)\Big], \quad \text{and} \tag{A4b}$$

$$S_{vv} = K\Big[\alpha + (\alpha_{zb} - \alpha)(\cos^2\theta_i \sin^2\theta_b \sin^2\phi_b + \sin^2\theta_i \cos^2\theta_b) + \frac{\sin 2\theta_i \sin 2\theta_b \cos\phi_b}{2}\Big], \tag{A4c}$$

where θ_b is the angle of the symmetry axis with respect to the vertical z; ϕ_b is the angle of the symmetry axis projection on the horizontal plane and the x axis; θ_i is the incident angle (again with respect to z), and it is related to the antenna elevation angle el as $\theta_i = 90° - \text{el}$ (Bringi and Chandrasekar 2001, their Fig. 2.6); α is polarizability in the horizontal plane; α_{zb} is polarizability along the vertical (z) axis. The factor

$$K = \frac{k_0^2}{4\pi\varepsilon_0}, \tag{A5}$$

where k_0 is free space wavenumber and ε_0 is free space permittivity.

For fully random orientation of prolates in the horizontal plane $\theta_b = 90°$ and ϕ_b is uniformly distributed over a 360° interval (due to symmetry this is the same as uniform distribution over a 180° interval). With these conditions the second moments of the backscattering matrix coefficients are

$$\langle |S_{hh}|^2 \rangle = \langle |S_{vv}|^2 \rangle = \frac{K^2}{\pi}\int_0^{\pi} |\alpha + (\alpha_{zb} - \alpha)\sin^2\phi_b|^2 \, d\phi_b, \tag{A6a}$$

$$\langle |S_{hv}|^2 \rangle = \frac{K^2}{4\pi}\int_0^{\pi} |(\alpha_{zb} - \alpha)\sin 2\phi_b|^2 \, d\phi_b, \tag{A6b}$$

$$\langle S_{hh}^* S_{hv} \rangle = \frac{K^2}{\pi}\int_0^{\pi} [\alpha + (\alpha_{zb} - \alpha)\sin^2\phi_b]^* \times [(\alpha_{zb} - \alpha)\sin 2\phi_b] \, d\phi_b, \quad \text{and} \tag{A6c}$$

$$\langle S_{hh}^* S_{vv} \rangle = \frac{K^2}{\pi}\int_0^{\pi} [\alpha + (\alpha_{zb} - \alpha)\sin^2\phi_b]^* \times [\alpha + (\alpha_{zb} - \alpha)\cos^2\phi_b] \, d\phi_b. \tag{A6d}$$

Note that the magnitudes in these equations are required if complex permittivity is used, which, however, we will not do because the addition of the imaginary part makes little difference.

Next we integrate (A6) to obtain

$$\frac{\langle |S_{hh}|^2 \rangle}{K^2} = |\alpha|^2 + \text{Re}[\alpha^*(\alpha_{zb} - \alpha)] + \frac{3}{8}|\alpha_{zb} - \alpha|^2, \tag{A7a}$$

$$\frac{\langle |S_{hv}|^2 \rangle}{K^2} = \frac{|\alpha_{zb} - \alpha|^2}{8}, \tag{A7b}$$

$$\langle S_{hh}^* S_{hv} \rangle = 0, \quad \text{and} \tag{A7c}$$

$$\frac{\langle S_{hh}^* S_{vv} \rangle}{K^2} = |\alpha|^2 + \text{Re}[\alpha^*(\alpha_{zb} - \alpha)] + \frac{1}{8}|\alpha_{zb} - \alpha|^2. \tag{A7d}$$

By inspection $\langle |S_{hh}|^2 \rangle > \langle |S_{hv}|^2 \rangle$ and therefore $L_{dr} < 1$. Moreover, in addition to $\langle S_{hh}^* S_{hv} \rangle = 0$, $\langle S_{vv}^* S_{hv} \rangle$ is also zero. Be aware that the inequality $L_{dr} < 1$ applies to the melting layer at vertical incidence but is not universally valid.

Next, derive a relation between the magnitudes of the measured correlation coefficient, ρ_{hvM} in the bright band and the intrinsic correlation coefficient, ρ_{hvi}. We start by multiplying (11b) with $\exp(-j\Phi_{DPsys})$ and take the magnitudes squared of each side. Then substitute the powers P_{hM} and P_{vM} from (10) and the correlation R_{hvM} from (11a) to get

$$|\rho_{hvM}|^2 = \frac{|\langle S_{hh}^* S_{vv} \rangle + \langle |S_{hv}|^2 \rangle e^{-j2\beta}|^2}{(\langle |S_{hh}|^2 \rangle + C_T^2 \langle |S_{hv}|^2 \rangle)(\langle |S_{hv}|^2 \rangle + C_T^2 \langle |S_{hh}|^2 \rangle)}. \tag{A8}$$

Insert L_{dr} from (21b) and $\rho_{hvi} = \langle S_{hh}^* S_{vv} \rangle / \langle |S_{hh}|^2 \rangle$ into (A8) so that

$$|\rho_{hvM}|^2 = \rho_{hvi}^2 \frac{|1 + L_{dr} e^{-j2\beta}/(1 - 2L_{dr})|^2}{(1/C_T^2 + L_{dr})(L_{dr} + C_T^2)} = \rho_{hvi}^2 F^2(\beta, L_{dr}), \tag{A9}$$

where F^2 is a fraction multiplying ρ_{hvi}^2, and it indicates how close $|\rho_{hvM}|$ is to ρ_{hvi}. For illustration assume that the transmitted powers are well balanced and hence $C_T^2 = 1$ and that the L_{DR} (dB) is between −11.5 and −13.7 dB as in the Fig. 11b dashed curve (i.e., $L_{dr1} = 0.0708$ and $L_{dr2} = 0.0427$ corresponding to $\rho_{hv1} = 0.858$ and $\rho_{hv2} = 0.915$). The fractions F at the two values of L_{dr} versus the transmitted differential phase are symmetric (Fig. A1) and for β in the interval from about −40° to 40° the Fs are between about 0.95 and 1.01. Then the $\max(\rho_{hvM}) = 0.915 \times 1.01 \approx 0.92$ and the $\min(\rho_{hvM}) = 0.858 \times 0.95 \approx 0.81$. Therefore, it follows from our data that if $\beta \in [-40°, 40°]$ and $\rho_{hvM} \in [0.81, 0.92]$ the

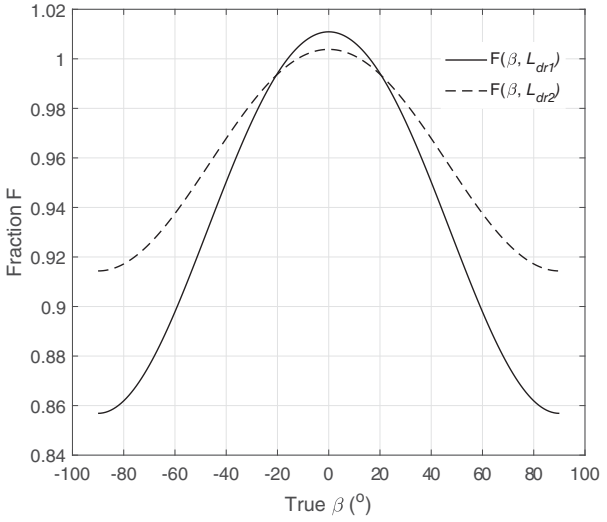

FIG. A1. The fraction F as function of β for $L_{\rm dr1} = 0.0708$ and $L_{\rm dr2} = 0.0427$ that cover the range measured in our data.

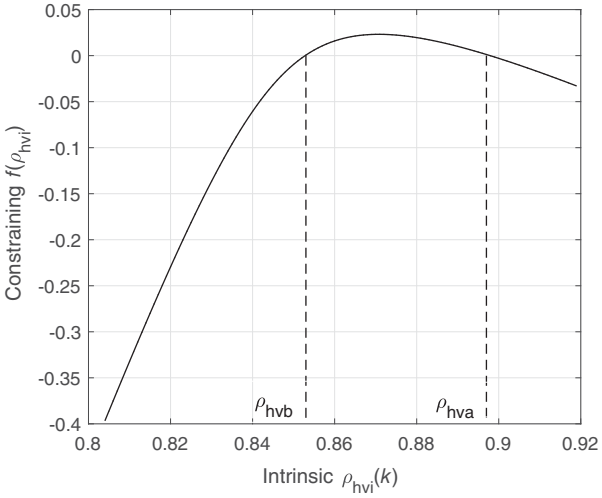

FIG. A2. Constraining function for solution 1 vs the intrinsic $\rho_{\rm hvi}$. The ambiguous solutions $\rho_{{\rm hv}b}$ and $\rho_{{\rm hv}a}$ are at the intersections of the dashed line and the abscissa.

$\rho_{\rm hvM}$ can be used in lieu of $\rho_{\rm hvi}$ for computing β. In that case the error in the β estimate is about 5°.

d. Ambiguity resolution

To resolve the ambiguity in β, we will use the moments (A7a), (A7b), and (A7d) and the intrinsic correlation coefficient

$$\rho_{\rm hvi} = \frac{\langle S_{\rm hh}^* S_{\rm vv}\rangle}{\langle |S_{\rm hh}|^2\rangle} = \frac{|\alpha|^2 + {\rm Re}[\alpha(\alpha_{zb} - \alpha)] + \frac{1}{8}|\alpha_{zb} - \alpha|^2}{|\alpha|^2 + {\rm Re}[\alpha(\alpha_{zb} - \alpha)] + \frac{3}{8}|\alpha_{zb} - \alpha|^2}. \tag{A10}$$

To do that we need the polarizabilities [Bringi and Chandrasekar 2001, their (240) and (A1.22a)]

$$\alpha = \frac{1}{[(\varepsilon_r - 1)(1 - \lambda_z)/2] + 1} \quad \text{and} \tag{A11a}$$

$$\alpha_{zb} = \frac{1}{(\varepsilon_r - 1)\lambda_z + 1}, \tag{A11b}$$

where ε_r is the relative permittivity and

$$\lambda_z = \frac{1 - e^2}{e^2}\left(-1 + \frac{1}{2e}\ln\frac{1 + e}{1 - e}\right). \tag{A12}$$

Here eccentricity $e = a/b$; b is the symmetry axis length and a is the small axis length (i.e., $a/b < 1$). In (A11) we have omitted the multiplying factor $V[\varepsilon_0(\varepsilon_r - 1)]$ that is in Bringi and Chandrasekar (2001) because it is a constant that in the expression for powers and correlation we absorb into C.

The closed form solutions for the second-order moments (A7) is handy for computing their dependence on β, that is, the forward operators. Thus, we set out to mimic results from scan 1. For that we need permittivity and axis ratio of the model prolates. Assume snowflakes are wet with relative permittivity of water $\varepsilon_r = 40$ at 3 cm wavelength. We ignore the imaginary part of relative permittivity as its effects are insignificant. A good match between observed correlation coefficient and modeled one occurs for equal mixture of two prolates, one with axis ratio 0.52, the other 0.595. Inserting these parameters into (A7) enables computation of $\rho_{\rm hvi}$ from (A10), $\rho_{\rm hvM}$ from (11b) as well as x, and y according to (14a) and (14b); C has no effect on the results, hence is set to 1. With the listed parameters we have generated the constraining $f[\rho_{\rm hvi}(k)]$, (24a) for solution 1 (Fig. A2) and show the two zero crossings: one yielding $\rho_{{\rm hv}a}$, the other $\rho_{{\rm hv}b}$. The main purpose of the figure is to illustrate that the modeled solutions resemble the ones from data in Fig. 5.

Next, we use the model to resolve the ambiguity between β corresponding to these two (a, b) options. Thus, we plot β_a and β_b versus true β using relations from the main text and (A7) as follows. We ignore the imbalances and absolute gains; therefore, $A = C = 1$. Then

$$\begin{aligned} P_{\rm hM} &= P_{\rm vM} = \langle |S_{\rm hh}|^2\rangle + \langle |S_{\rm hv}|^2\rangle \\ &= x_1[\rho_{\rm hvi}(k)] + y_1[\rho_{\rm hvi}(k)], \end{aligned} \tag{A13a}$$

$$\begin{aligned} D_M + jG_M &= \langle |S_{\rm hh}|^2\rangle \rho_{\rm hvi} + \langle |S_{\rm hv}|^2\rangle e^{-j2\beta} \\ &= x_1[\rho_{\rm hvi}(k)]\rho_{\rm hvi} + y_1[\rho_{\rm hvi}(k)]e^{-j2\beta}, \end{aligned} \tag{A13b}$$

$$\rho_{\rm hvi}(k) = 1 - 2y_1[\rho_{\rm hvi}(k)]/x_1[\rho_{\rm hvi}(k)], \quad \text{and} \tag{A13c}$$

$$\beta_n = \left[\arctan\left(-\frac{G_{\rm M}}{D_M - Ax_1[\rho_{\rm hvi}(k_s)]}\right)\right]\Big/2. \tag{A13d}$$

In (A13d) the index n stands for a or b to distinguish between these two possibilities. We vary the true β [exponent in (A13b)] between −90° and 0°; we exclude the positive values because the sign of the imaginary part on the left

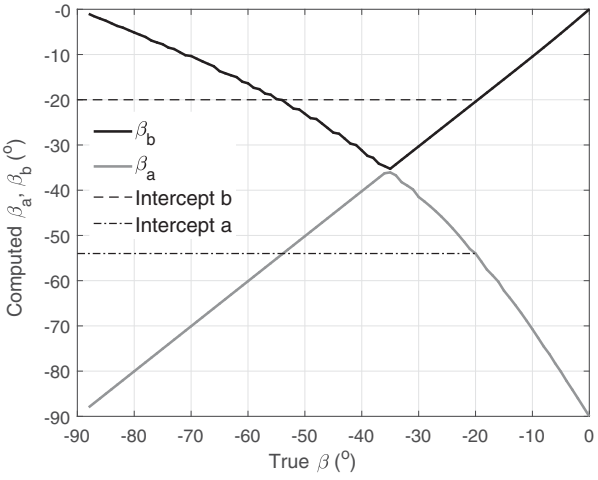

FIG. A3. Computed β_a and β_b as functions of true β for the melting layer modeled as equal mixture of two prolates. The dashed and dash–dotted lines indicate the two ambiguous solutions (−20° and −54°) for a true $\beta = -20°$.

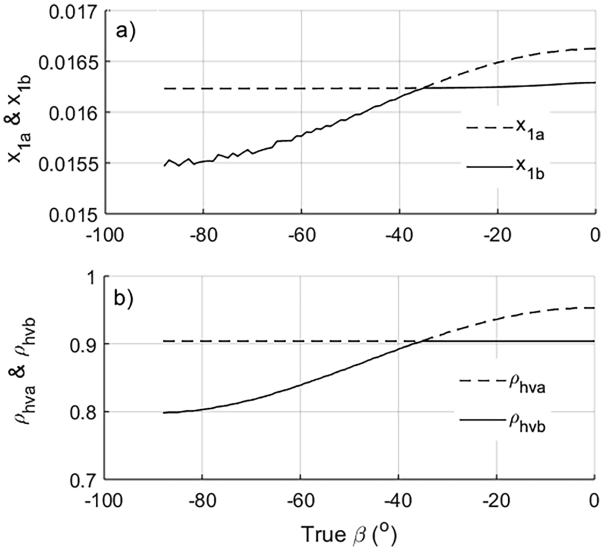

FIG. A4. (a) Solutions x_{1a} and x_{1b} as functions of β. The straight line (dashed changing to solid) at 0.001 624 is the correct x_1, whereas the curve represents the ambiguous x_1. (b) Solutions ρ_{hva} and ρ_{hvb} as functions of β. The straight line (dashed changing to solid) at 0.904 is the correct ρ_{hv}, whereas the curve represents the ambiguous ρ_{hv}.

side and the one on the right side of (A13b) in our data indicate that β must be negative. For each β we solve for ρ_{hva}, ρ_{hvb}, the corresponding pairs (x_{1a}, y_{1a}), (x_{1b}, y_{1b}), and (β_a, β_b).

The graphs of β_a and β_b (Fig. A3) show the ambiguity. For example, true $\beta = -20°$ (on the abscissa) corresponds to computed (measured) $\beta_a = -54°$ and $\beta_b = -20°$; similarly, the computed $\beta_b = -20°$ (on the ordinate) could have been caused by either measured $\beta_a = -54°$ or $\beta_b = -20°$. Clearly, additional information should be sought to identify the correct solution. A possible clue is the difference in slopes of these "transfer" functions. Having this in mind in search for a resolution, we plot in Fig. A4a, x_{1a}, x_{1b} and in Fig. A4b, ρ_{hva} and ρ_{hvb}.

The correct values from the model are represented with the straight lines in Figs. A4a and A4b, and the changing curves correspond to the wrong solution. Therefore, a way to determine which one, β_a or β_b, is the correct one is by examining the slopes of either ρ_{hvi} or x_1. This can be done on the data by changing the estimated $\Phi_{DPsys} = \beta + \gamma$, because changing it is equivalent to changing β. In addition, we can examine the changes in ρ_{hvi} or x_1 from scan to scan. Whichever of these two changes more indicates that it is a wrong solution. We have made these tests on our data and determined that the solution b is correct.

e. Depolarization

To compute depolarization ratios, the transmitted (H and V) polarized signals should have equal power and the receiver should be balanced. These two conditions are satisfied if $C_T = C_R = 1$ in which case (A1) becomes

$$V_h = C[S_{hh}e^{-j\Phi_{DP}} + S_{hv}e^{-j(\Phi_{DP}/2-\beta)}] \quad \text{and} \tag{A14a}$$

$$V_v = C[S_{hv}e^{-j(\Phi_{DP}/2-\gamma)} + S_{vv}e^{j(\beta+\gamma)}]. \tag{A14b}$$

Assume negligible differential phase on propagation, multiply the equation pair (A14) with $e^{-j(\beta+\gamma)}$ so that $V_h^c = V_h e^{-j(\beta+\gamma)}$ and $V_v^c = V_v e^{-j(\beta+\gamma)}$, and then form the depolarization ratio D_{dr},

$$D_{dr} = \frac{\langle |V_h^c - V_v^c|^2 \rangle}{\langle |V_h^c + V_v^c|^2 \rangle} = \frac{\langle |S_{hh}e^{-j(\beta+\gamma)} + S_{hv}e^{-j\gamma} - S_{hv}e^{-j\beta} - S_{vv}|^2 \rangle}{\langle |S_{hh}e^{-j(\beta+\gamma)} + S_{hv}e^{-j\gamma} + S_{hv}e^{-j\beta} + S_{vv}|^2 \rangle}. \tag{A15}$$

This equation is analogous to (11) in Matrosov (2004), but we use opposite signs on β and γ. Moreover, we ignore attenuation, and he does not. We alert readers that the operation on voltages in (A15) is from pulse to pulse.

REFERENCES

Barge, B., 1974: Polarization measurements of precipitation backscatter in Alberta. *J. Rech. Atmos.*, **8**, 163–173.

Borowska, L., and D. S. Zrnić, 2012: Use of ground clutter to monitor polarimetric radar calibration. *J. Atmos. Oceanic Technol.*, **29**, 159–176, https://doi.org/10.1175/JTECH-D-11-00036.1.

Bringi, V. N., and V. Chandrasekar, 2001: *Polarimetric Doppler Weather Radar*. Cambridge University Press, 636 pp.

Bukovčić, P., A. Ryzhkov, and D. Zrnić, 2020: Polarimetric relations for snow estimation—Radar verification. *J. Appl. Meteor. Climatol.*, **59**, 991–1009, https://doi.org/10.1175/JAMC-D-19-0140.1.

Cao, Q., M. Knight, A. V. Ryzhkov, P. Zhang, and N. E. Lawrence, III, 2017: Differential phase calibration of linearly

polarized weather radars with simultaneous transmission/reception for estimation of circular depolarization ratio. *IEEE Trans. Geosci. Remote Sens.*, **55**, 491–501, https://doi.org/10.1109/TGRS.2016.2609421.

Carlin, J. T., J. Gao, J. C. Snyder, and A. V. Ryzhkov, 2017: Assimilation of Z_{DR} columns for improving the spinup and forecast of convective storms in storm-scale models: Proof-of-concept experiments. *Mon. Wea. Rev.*, **145**, 5033–5057, https://doi.org/10.1175/MWR-D-17-0103.1.

Chandrasekar, V., J. Hubbert, V. N. Bringi, and P. F. Meishner, 1994: Analysis and interpretation of dual-polarized radar measurements at +45° and −45° linear polarization states. *J. Atmos. Oceanic Technol.*, **11**, 323–336, https://doi.org/10.1175/1520-0426(1994)011<0323:AAIODP>2.0.CO;2.

Doviak, R. J., and D. S. Zrnić, 1998: NOAA/NSSL's WSR-88D radar for research and enhancement of operations: Polarimetric upgrades to improve rainfall measurements. NSSL Tech. Rep., 110 pp., https://www.nssl.noaa.gov/publications/wsr88d_reports/2pol_upgrades.pdf.

——, V. Bringi, A. Ryzhkov, A. Zahrai, and D. S. Zrnić, 2000: Considerations for polarimetric upgrades of operational WSR-88D radars. *J. Atmos. Oceanic Technol.*, **17**, 257–278, https://doi.org/10.1175/1520-0426(2000)017<0257:CFPUTO>2.0.CO;2.

Frech, M., M. Hagen, and T. Mammen, 2017: Monitoring the absolute calibration of a polarimetric weather radar. *J. Atmos. Oceanic Technol.*, **34**, 599–615, https://doi.org/10.1175/JTECH-D-16-0076.1.

Galletti, M., and D. S. Zrnić, 2011: Bias in copolar correlation coefficient caused by antenna radiation patterns. *IEEE Trans. Geosci. Remote Sens.*, **49**, 2274–2280, https://doi.org/10.1109/TGRS.2010.2095019.

Gorgucci, E., G. Scarchilli, and V. Chandrasekar, 1999: A procedure to calibrate multiparameter weather radar using properties of the rain medium. *IEEE Trans. Geosci. Remote Sens.*, **37**, 269–276, https://doi.org/10.1109/36.739161.

Krause, J. M., 2016: A simple algorithm to discriminate between meteorological and nonmeteorological radar echoes. *J. Atmos. Oceanic Technol.*, **33**, 1875–1885, https://doi.org/10.1175/JTECH-D-15-0239.1.

Matrosov, S. Y., 2004: Depolarization estimates from linear H and V measurements with weather radars operating in simultaneous transmission–simultaneous receiving mode. *J. Atmos. Oceanic Technol.*, **21**, 574–583, https://doi.org/10.1175/1520-0426(2004)021<0574:DEFLHA>2.0.CO;2.

——, R. F. Reinking, R. A. Kropfli, B. E. Marner, and B. W. Bartam, 2001: On the use of radar depolarization ratios for estimating shapes of ice hydrometeors in winter clouds. *J. Appl. Meteor.*, **40**, 479–490, https://doi.org/10.1175/1520-0450(2001)040<0479:OTUORD>2.0.CO;2.

——, G. G. Mace, R. Marchand, M. D. Shupe, A. G. Hallar, and I. B. McCubbin, 2012: Observations of ice crystal habits with a scanning polarimetric W-band radar at slant linear depolarization ratio mode. *J. Atmos. Oceanic Technol.*, **29**, 989–1008, https://doi.org/10.1175/JTECH-D-11-00131.1.

——, C. G. Schmitt, M. Maahn, and G. de Boer, 2017: Atmospheric ice particle shape estimates from polarimetric radar measurements and in situ observations. *J. Atmos. Oceanic Technol.*, **34**, 2569–2587, https://doi.org/10.1175/JTECH-D-17-0111.1.

Melnikov, V., 2020: Impacts of the phase shift between incident radar waves on the polarization variables from ice cloud particles. *J. Atmos. Oceanic Technol.*, **37**, 1423–1436, https://doi.org/10.1175/JTECH-D-19-0197.1.

——, and S. Y. Matrosov, 2013: Estimations of aspect ratios of ice cloud particles with the WSR-88D radar. *36th Conf. on Radar Meteorology*, Breckenridge, CO, Amer. Meteor. Soc., 245, https://ams.confex.com/ams/36Radar/webprogram/Paper228291.html.

——, M. J. Istok, and J. K. Westbrook, 2015: Asymmetric radar echo patterns from insects. *J. Atmos. Oceanic Technol.*, **32**, 659–674, https://doi.org/10.1175/JTECH-D-13-00247.1.

Moisseev, D. N., C. M. H. Unal, H. W. J. Russchenberg, and L. P. Ligthart, 2002: Improved polarimetric calibration for atmospheric radars. *J. Atmos. Oceanic Technol.*, **19**, 1968–1977, https://doi.org/10.1175/1520-0426(2002)019<1968:IPCFAR>2.0.CO;2.

Park, H. S., A. V. Ryzhkov, D. S. Zrnić, and K.-E. Kim, 2009: The hydrometeor classification for the polarimetric WSR-88D: Description and application to an MCS. *Wea. Forecasting*, **24**, 730–748, https://doi.org/10.1175/2008WAF2222205.1.

Peters, G., B. Fischer, H. Münster, M. Clemens, and A. Wagner, 2005: Profiles of raindrop size distributions as retrieved by microrain radars. *J. Appl. Meteor.*, **44**, 1930–1949, https://doi.org/10.1175/JAM2316.1.

Reinking, R. F., S. Y. Matrosov, R. A. Kropfli, and B. W. Bartram, 2002: Evaluation of a 45° slant quasi-linear radar polarization state for distinguishing drizzle droplets, pristine ice crystals, and less regular ice particles. *J. Atmos. Oceanic Technol.*, **19**, 296–321, https://doi.org/10.1175/1520-0426-19.3.296.

Ryzhkov, A. V., and D. S. Zrnić, 2019: *Radar Polarimetry for Weather Observations*. Springer Atmospheric Sciences, Springer, 486 pp.

——, and Coauthors, 2017: Estimation of depolarization ratio using weather radars with simultaneous transmission/reception. *J. Appl. Meteor. Climatol.*, **56**, 1797–1816, https://doi.org/10.1175/JAMC-D-16-0098.1.

——, J. Snyder, J. T. Carlin, A. Khain, and M. Pinsky, 2020: What polarimetric weather radars offer to cloud modelers: Forward radar operators and microphysical/thermodynamic retrievals. *Atmosphere*, **11**, 362, https://doi.org/10.3390/atmos11040362.

Schroth, A. C., M. S. Chandra, and P. F. Meischner, 1988: A C-band coherent polarimetric radar for propagation and cloud physics research. *J. Atmos. Oceanic Technol.*, **5**, 803–822, https://doi.org/10.1175/1520-0426(1988)005<0803:ABCPRF>2.0.CO;2.

Straka, J. M., D. S. Zrnić, and A. V. Ryzhkov, 2000: Bulk hydrometeor classification and quantification using polarimetric radar data: Synthesis of relations. *J. Appl. Meteor.*, **39**, 1341–1372, https://doi.org/10.1175/1520-0450(2000)039<1341:BHCAQU>2.0.CO;2.

Sullivan, A., 1889: *The Gondoliers: Or The King of Barataria*. Act II.

Zhang, G., and Coauthors, 2019: Current status and future challenges of weather radar polarimetry: Bridging the gap between radar meteorology/hydrology/engineering and numerical weather prediction. *Adv. Atmos. Sci.*, **36**, 571–588, https://doi.org/10.1007/s00376-019-8172-4.

Zhang, J., L. Tang, S. Cocks, P. Zhang, A. Ryzhkov, K. Howard, C. Langston, and B. Kaney, 2020: A dual-polarization radar synthetic QPE for operations. *J. Hydrometeor.*, **21**, 2507–2521, https://doi.org/10.1175/JHM-D-19-0194.1.

Zrnić, D. S., N. Balakrishnan, A. V. Ryzhkov, and S. L. Durden, 1994a: Use of copolar correlation coefficient for probing

precipitation at nearly vertical incidence. *IEEE Trans. Geosci. Remote Sens.*, **32**, 740–748, https://doi.org/10.1109/36.298003.

——, R. Raghavan, and V. Chandrasekar, 1994b: Observation of copolar correlation coefficient through a bright band at vertical incidence. *J. Appl. Meteor.*, **33**, 45–52, https://doi.org/10.1175/1520-0450(1994)033<0045:OOCCCT>2.0.CO;2.

——, R. Doviak, G. Zhang, and A. Ryzhkov, 2010: Bias in differential reflectivity due to cross coupling through the radiation patterns of polarimetric weather radars. *J. Atmos. Oceanic Technol.*, **27**, 1624–1637, https://doi.org/10.1175/2010JTECHA1350.1.